Science Advances
AAAS

advances.sciencemag.org/cgi/content/full/6/15/eaaz4948/DC1

Supplementary Materials for

A general approach for hysteresis-free, operationally stable metal halide perovskite field-effect transistors

Satyaprasad P. Senanayak, Mojtaba Abdi-Jalebi, Varun S. Kamboj, Remington Carey, Ravichandran Shivanna, Tian Tian, Guillaume Schweicher, Junzhan Wang, Nadja Giesbrecht, Daniele Di Nuzzo, Harvey E. Beere, Pablo Docampo, David A. Ritchie, David Fairen-Jimenez, Richard H. Friend, Henning Sirringhaus*

*Corresponding author. Email: hs220@cam.ac.uk

Published 10 April 2020, *Sci. Adv.* **6**, eaaz4948 (2020)
DOI: 10.1126/sciadv.aaz4948

This PDF file includes:

Sections S1 to S14
Figs. S1 to S37
Tables S1 and S2

S1. Characterization of the perovskite films

In order to optimize the perovskite FET performance, films were fabricated using two methods: the first one involved spinning the precursor at 5000 rpm for 180 seconds and annealing at 100 ^{0}C for 30 minutes, and the second method involved spinning the precursor solution at 5000 rpm for 180 seconds with an anti-solvent chlorobenzene introduced at 6 seconds ($FAMAPbI_3$ perovskite) or 30 seconds ($CsFAMAPbI_3$ and $RbCsFAMAPbI_3$).

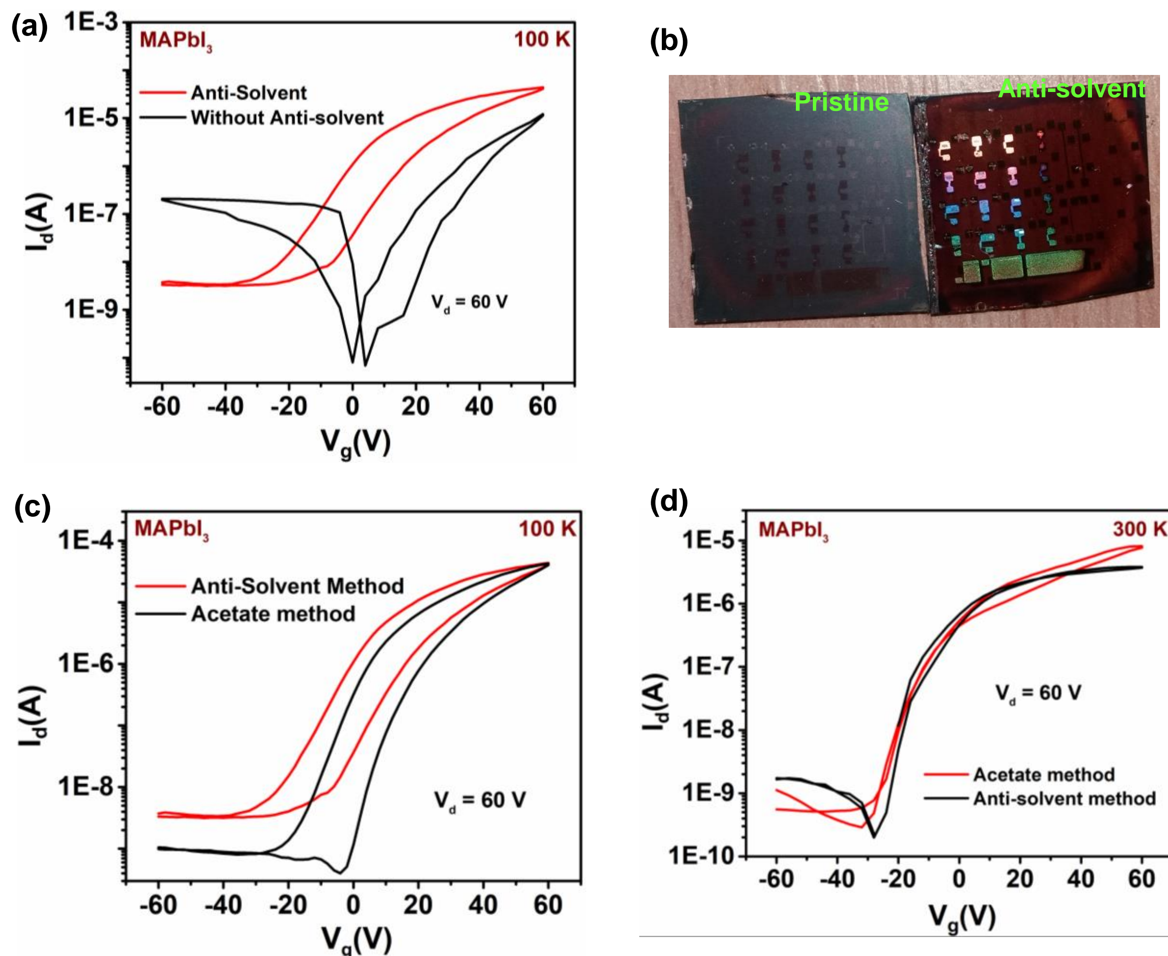

Figure S1: Anti-solvent method for perovskite FETs. Transfer characteristics measured at 100 K on a top-gate, bottom-contact perovskite FET fabricated with $MAPbI_3$ perovskite films (L = 20 μm, W = 1mm). (a) Spin-coated with (red) and without the anti-solvent (black) method. (b) Optical image of the devices depicting a shiny smooth film formed upon solvent treatment. Comparison of transfer characteristics for devices fabricated from PbI_2 based precursor along with anti-solvent method (red) and with $Pb(Ac)_2$ precursor (black) at (c) 100 K and (d) 300 K.

Perovskite FETs fabricated with the anti-solvent method exhibit at least an order of magnitude increase in the channel current (**Figure S1a**). Moreover, the devices fabricated from perovskite films fabricated without the anti-solvent method (optical image in **Figure S1b**) exhibit no field effect modulation when operated at room temperature. Hence, all the FETs reported here were fabricated from perovskite films prepared with the anti-solvent method. Nevertheless, as shown in **figure S1c** and **d** the transfer characteristics of $MAPbI_3$ FETs exhibit a similar level of channel current when fabricated with PbI_2 precursor with the help of the anti-solvent technique as devices fabricated from $Pb(Ac)_2$ precursor *(25)*.

S2. Effect of the dipole moment of A-cation on FET characteristics

Perovskite FETs exhibit hysteretic characteristics both at low temperature and high temperature which is attributed to both the dipolar character of the A-cation and the presence of migrating ionic defects. This is evident from the observation of the hysteresis in the output characteristics (**Figure S2**).

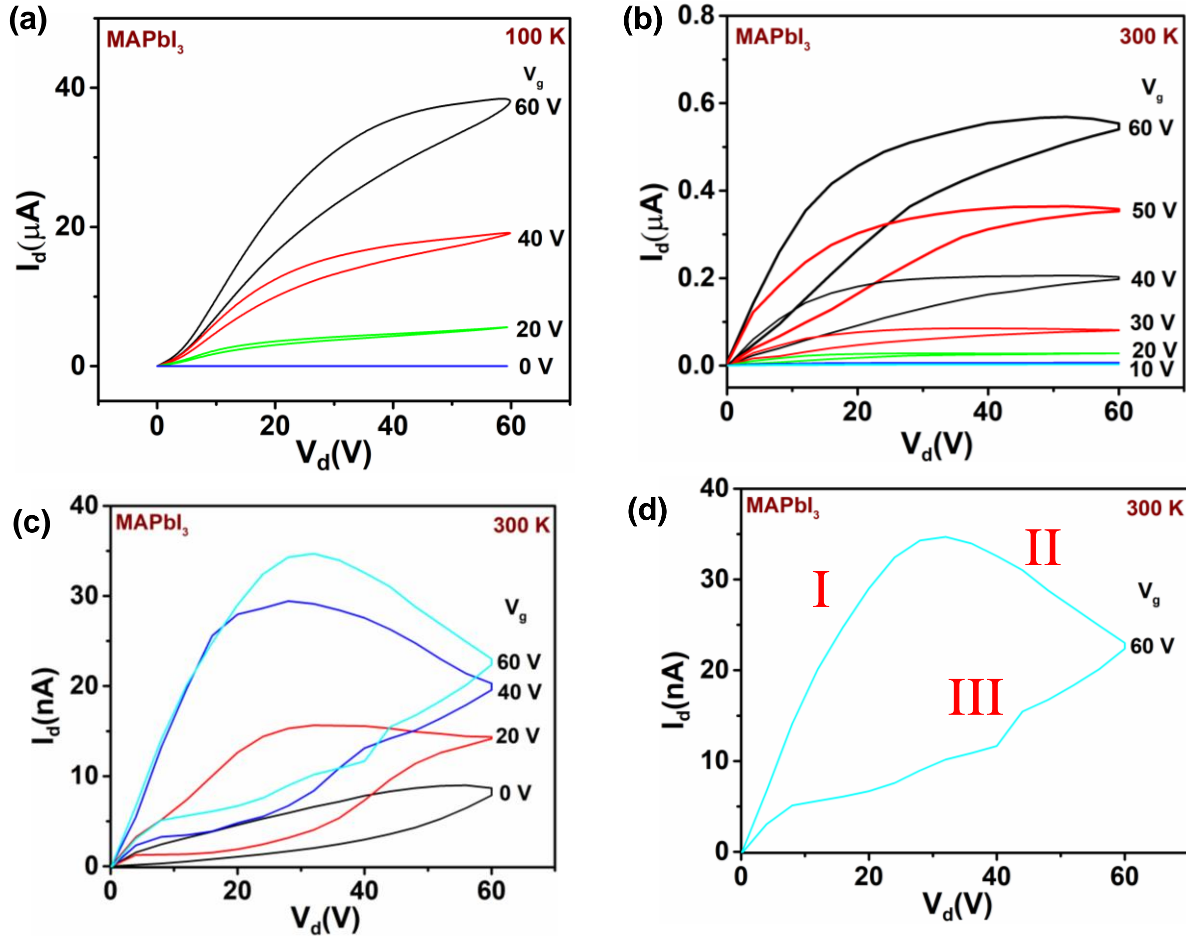

Figure S2: Effect of temperature and channel length on the output characteristics.(a) Output characteristics measured at 100 K on a top-gate, bottom-contact $MAPbI_3$ perovskite FET fabricated with L = 20 μm. Measured output characteristics for $MAPbI_3$ FETs at 300 K for devices with (b) L = 100 μm, W = 1mm (c) L = 20 μm, W = 1mm. (d) Zoomed in output characteristics depicting different regimes of transport.

The complex hysteretic behaviour observed in the output characteristics (**Figure S2**) can mainly be attributed to ionic defect migration/screening of the gate potential. The forward sweep (region I) of the output characteristic corresponds to the near ideal transistor characteristic with a defined linear regime (**Figure S2d**). Upon increasing the V_d when the conduction in the channel increases the channel current is expected to reach saturation. However, due to the application of V_g ionic defect is expected to screen the gate potential

which effectively causes the channel current to decrease as the measurement progresses (region II). The region III of the graph corresponds to the reverse sweep in the drain bias from 60 V to 0 V. Under this condition with applied V_g, ion movement is expected in these perovskite FETs. The movement of negative ions in the perovskite towards the active interface would screen the gate potential. As negative ions migrate towards the interface and screen the gate voltage, positive ions will migrate into the bulk/towards the backchannel interface, where the associated space charge will facilitate the formation of this parallel electron conduction channel. In the reverse sweep (regime III), the charge transport becomes completely controlled by the second conduction channel, as the field-effect channel at the interface is most likely fully screened after the prolonged application of the positive gate bias.

One important observation which can also be made from the output characteristics measured on $MAPbI_3$ devices shown in **figure 1 and S2** is that the degree of hysteresis in the output characteristics improves upon increasing the channel length. This decrease in contact resistance becomes evident upon comparing the contact resistance estimated from the transfer line method in the forward sweep of the output characteristics (**Figure S3**).

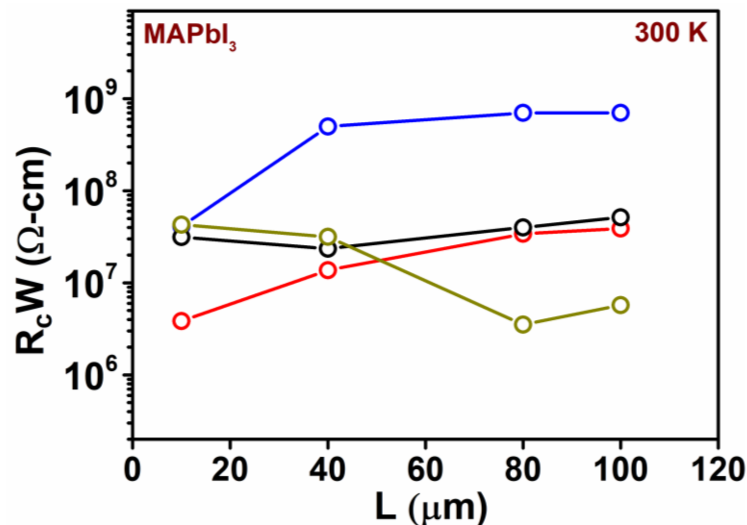

Figure S3: Contact resistance estimation. Transmission line measurements of the normalized channel resistance as a function of channel length for FETs comprising $MAPbI_3$ for different batches of devices. The contact resistance can be extracted from extrapolation to zero channel length.

As observed in figure S3, there is a spread in the transmission line measurement data. The channel resistance is obtained from a linear fit to the output curves measured at different channel length and the contact resistance is obtained by extrapolating this plot to zero channel length. The spread in contact resistance originates because the output curves are generally more susceptible to the effects of ion migration and this is why we have extracted mobilities

from the saturated transfer characteristics of the perovskite devices. To understand this we compare the channel current between the output and the transfer characteristics under similar bias condition. We define the I_{ds} mismatch parameter $(\xi) \equiv I_{ds}^{transfer}/I_{ds}^{output}$ at the same voltage condition (here $V_d = V_g = 60$ V); for a perfectly stable FET ξ is expected to be 1.This mismatch is larger for perovskite FETs fabricated with smaller channels ($\xi \sim 10 - 50$) for $MAPbI_3$ devices fabricated with smaller channel length L = 20 µm and decreases to $\xi \sim 5$ for devices with L = 100 µm.

Nevertheless, to understand the origin of the residual hysteresis at 100 K (where ionic defect migration is expected to be negligible) we compared the output characteristics of $MAPbI_3$ at 100K (**Figure S2a**) with those of $FAPbI_3$ (**Figure S4**).

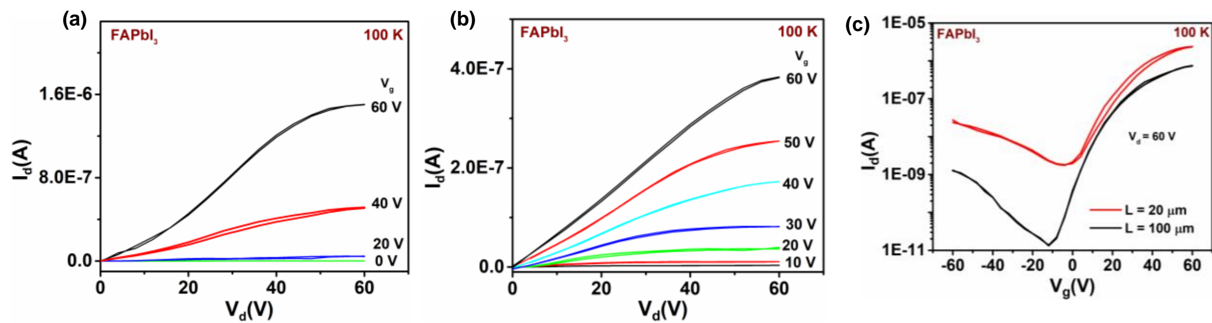

Figure S4: $FAPbI_3$ FETs. Output characteristics measured at 100 K on a top-gate bottom contact $FAPbI_3$ perovskite FETs fabricated with (a) L = 20 µm (b) L = 100 µm. Transfer characteristics measured on the same device with L = 20 µm (red) and L = 100 µm (black)

Note that $FAPbI_3$ devices exhibit negligible hysteresis in the output characteristics even for devices fabricated with L = 20 µm but exhibits a contact resistance limited characteristics. Upon increasing the channel length to 100 µm the output characteristics exhibit more ideal textbook like behaviour.

To understand this trend we characterized the dipole moment of the A-cation by impedance spectroscopy. For impedance measurements, we fabricated Au/Perovskite/Au sandwich structures with a thicker perovskite film fabricated from a 1.2 M solution of $MAPbI_3$ and $FAPbI_3$. To minimize leakage and obtain reliable devices, thicker perovskite films (> 0.35 µm) were used. Impedance measurements were performed using a standard Keithley 4200 SCS Parameter Analyzer using a small sinusoidal voltage of 30 mV; the frequency was swept over the range of 1 kHz to 10 MHz. Note that our measurement set up becomes unreliable above 3 MHz.

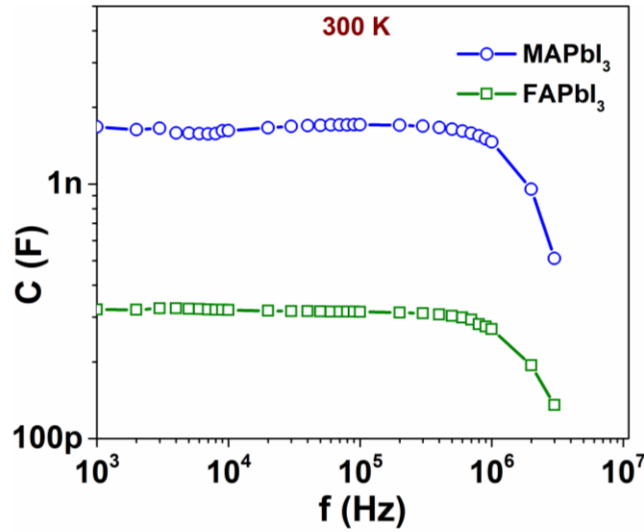

Figure S5: Impedance spectroscopy measured on the capacitor of a 350 nm perovskite thin film vertical device (area of 0.45 cm^2) with an AC voltage of 30 mV.

From the capacitance measurements, the dielectric constant is estimated to be $\varepsilon_r \sim 27$ (at 100 kHz) for $MAPbI_3$; this decreases to 4.3 (at 100 kHz) for $FAPbI_3$ (**Figure S5**). The dielectric behaviour of the perovskite can be modelled using the standard Kirkwood-Fröhlich equation for polar, orientationally disordered solids. Considering the entropic disorder of the A-cation at room temperature the Kirkwood correlation factor is equal to 1. Assuming that the optical dielectric constant of perovskite $\varepsilon_\infty \sim 6.5$ for $MAPbI_3$ (~ 5 for $FAPbI_3$) and the molar volume is 3.95×10^{27} m^{-3}, we obtain a dipole moment of 1.94 D for $MAPbI_3$, which decreases to 0.45 D for $FAPbI_3$ *(5,25,31)*. Note that the magnitude of the dipole moment estimated from impedance measurements is comparable to the dipole moment estimated from ab initio electronic structure calculations *(31)*.

$FAPbI_3$ devices fabricated at 300 K also exhibited nearly hysteresis-free transfer characteristics and improved output characteristics (**Figure S6**) compared to $MAPbI_3$ perovskite FETs (**Figure S2**)

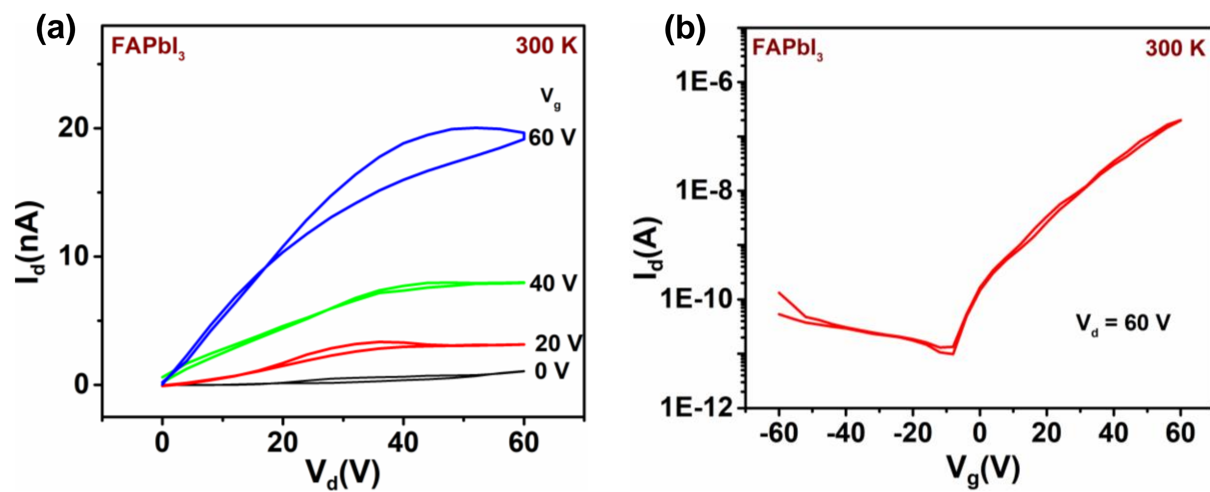

Figure S6: Room temperature characteristics of $FAPbI_3$ FETs.(a) Output characteristics and (b) transfer characteristics measured at 300 K on a top-gate, bottom-contact $FAPbI_3$ perovskite FET with L = 100 µm, W = 1mm.

S3. Characterization of $FAPbI_3$ films

Structural characterization of $FAPbI_3$ films were performed using X-ray diffraction measurements which were conducted on $FAPbI_3$ films fabricated on Si-substrates in a similar manner as used for device fabrication. The measurements were performed using a D8 Advance X-ray diffractometer (Bruker AXS, Karlsruhe, Germany) using a Cu K_α source (1.5418 Å). The incident beam slit width was 0.6 mm. Data for the experiments were collected in a locked-coupled 1D-mode for 2θ between 5° and 60°, with a step size of 0.004° integrated for 0.4 s/step on a Bruker Lynx-Eye detector. The final diffraction pattern is obtained upon normalizing for the background including the Si substrate. A Rietveld refinement was used to assign these Bragg-peaks, using the Full Proof Suite.

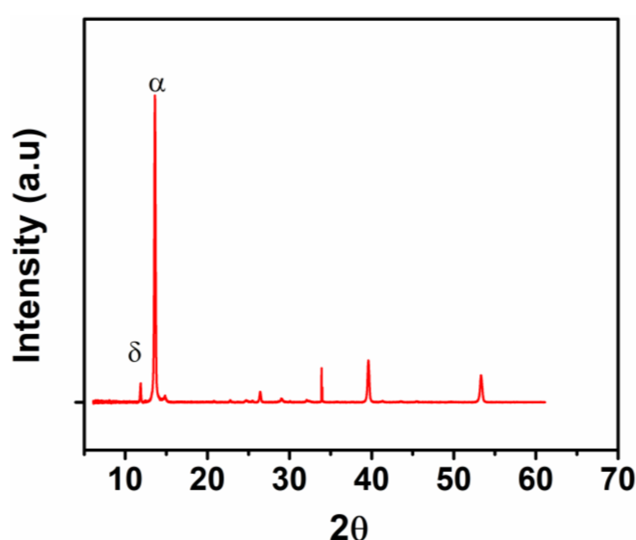

Figure S7: XRD pattern obtained from $FAPbI_3$ thin films.

In the XRD pattern shown in **figure S7**, we observe the existence of the peak at 11.8° which corresponds to the non-perovskite δ-$FAPbI_3$ phase. Based on the intensity difference between the peak at 11.8° and 13.9° we observe that only 5.7 % of $FAPbI_3$ is in the unconverted, non-perovskite phase *(25)*. A clear signature of the non-perovskite phase is also observed in photo-thermal deflection spectroscopy (PDS). We estimated the energetic disorder of the film using PDS, which is a sensitive absorption measurement of the tail of the optical absorption into the band gap. The samples were kept in an airtight-sealed quartz cuvette filled with an inert liquid, Fluorinert FC-72 obtained from 3M Corporation, which acts as the deflection medium with a large temperature-dependent refractive index. The perovskite thin films were excited with a modulated monochromatic light beam perpendicular to the plane of the sample obtained by a combination of a Light Support MKII 100W Xenon

arc source and a CVI DK240 monochromator. The transverse probe beam was produced with a Qioptiq 670-nm fiber-coupled diode laser and passed as close as possible to the perovskite film surface. Beam deflection was measured using a differentially amplified quadrant photodiode and a Stanford Research SR830 lock-in amplifier, which is proportional to the absorption in the sample. The energetic disorder is quantified using a parameter known as Urbach energy (E_u) by fitting the exponential drop in absorption at the band edge.

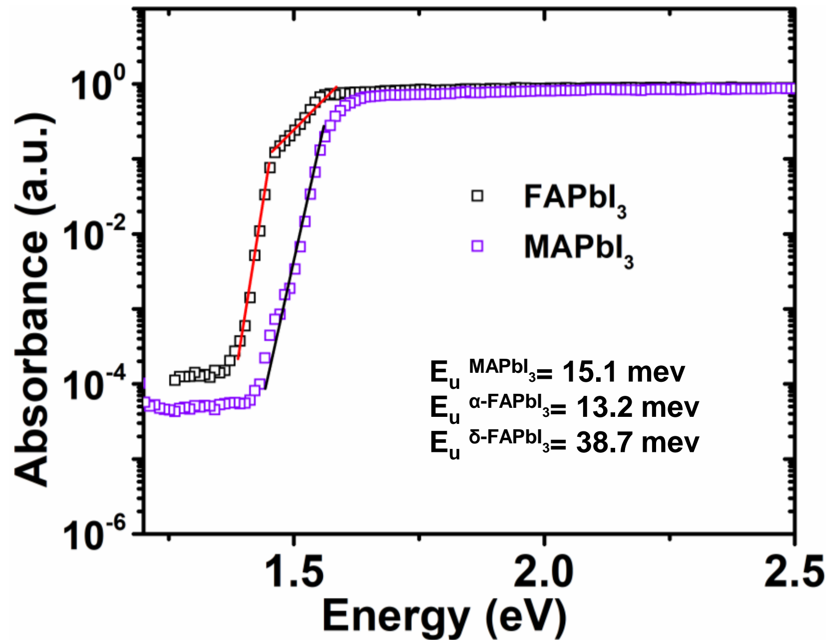

Figure S8: PDS measurement performed on $FAPbI_3$ and $MAPbI_3$ thin films made using the same method as used for device fabrication.

PDS measurements shown in **figure S8** shows the existence of a disordered phase (with E_u = 38.7 meV) attributed to the presence of the non-perovskite δ-$FAPbI_3$ phase along with the perovskite α-$FAPbI_3$ phase. The Urbach energy of the α-$FAPbI_3$ perovskite phase is slightly smaller (E_u = 13.2 meV) than that of the $MAPbI_3$ perovskite film (E_u = 15.1 meV) reflecting the reduced dipolar disorder due to the smaller A-cation dipole moment.

S4. Characterization of multi-cation perovskite films

Structural characterization: X-ray diffraction measurements were also conducted on the other perovskite films fabricated on Si-substrates in a similar manner as used for device fabrication. Rietveld refinement was used to assign these Bragg-peaks, using the Full Proof Suite. XRD patterns of the perovskite films exhibit clean characteristics with the absence of any peak corresponding to un-converted PbI_2. Moreover, the XRD patterns for $FAMAPbI_3$, $CsFAMAPbI_3$, $RbCsFAMAPbI_3$ do not exhibit any peak at 11.8° indicating the absence of yellow, non-perovskite δ-phase in these thin films (**Figure S9a**) *(35)*. Comparing $MAPbI_3$ with $RbCsFAMAPbI_3$ perovskite thin films the XRD peaks of the latter exhibit a decrease in FWHM by 15 % indicating improved crystalline order and grain size. To understand the effect of Rb concentration on the crystallinity and to obtain the optimized stoichiometry for developing high-performance perovskite FETs, XRD measurements were performed on perovskite films upon controllably varying the Rb concentration from 1% to 20 %. We observe a decrease in FWHM of the (110) peak upon increasing the concentration of up to 5 % (**Figure S9b**). However, upon increasing the concentration to more than 5% the FWHM increases. Furthermore, a clear signature of phase segregated $RbPbI_3$ is observed for Rb concentration above 10%.

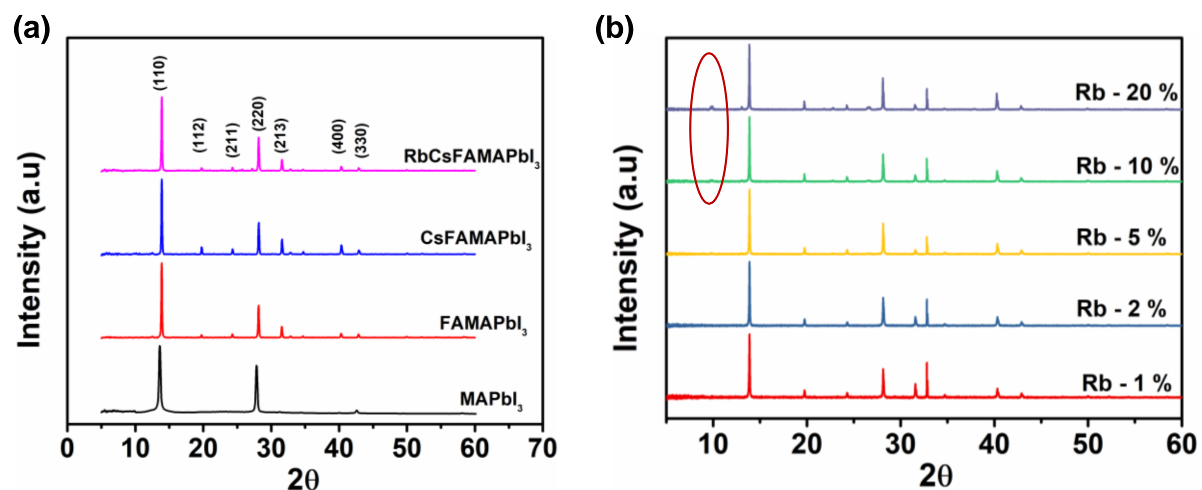

Figure S9: Structural analysis of perovskite films. (a) High resolution XRD patterns of perovskite thin films indicating phase pure perovskite formation with labelled characteristic peaks and absence of PbI_2 peak. (b) XRD patterns obtained upon gradual variation of the Rb concentration in $CsFAMAPbI_3$; the evolution of phase segregated $RbPbI_3$ is highlighted by the oval shape for concentrations above 10 %.

Microscopic Characterization:

Detailed microscopic characterization of the perovskite films fabricated with different multi-cationic mixtures was obtained using a FEI Philips Dualbeam Quanta 3D Scanning Electron Microscope (SEM). Considering the semiconducting properties of the perovskite films, the SEM images were taken at 5kV and at a working distance of 7.5 mm while ensuring that the process of SEM imaging does not cause any beam damage to the sample. SEM images shown in **figure S10** depict the formation of polycrystalline grains in all the perovskite films fabricated with the anti-solvent treatment. Note that the grain size increase from 150 nm in $MAPbI_3$ to 220 nm in Rb(5%)$CsFAMAPbI_3$ (consistent with the decrease in FWHM of the XRD pattern), the device performance improves consistently with the increase in grain size. Upon increasing the Rb concentration to 10% phase segregated $RbPbI_3$ grains are formed and the grain size decreases to 50 – 75 nm. Nevertheless, in agreement with the structural characterization in the microscopic characterization also we observe the formation of a phase segregated non-perovskite phase for Rb(10%)$CsFAMAPbI_3$ films.

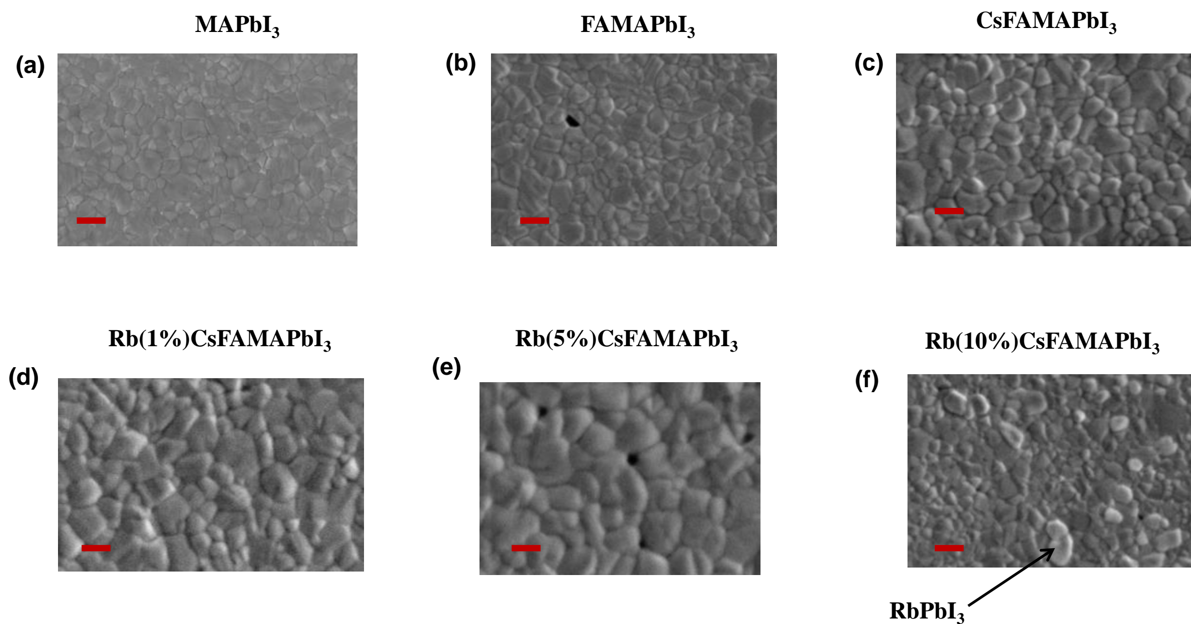

Figure S10: Microscopic Characterization. SEM measurement on different perovskite thin films (a) $MAPbI_3$; (b) $FAMAPbI_3$; (c) $CsFAMAPbI_3$; (d) Rb(1%)$CsFAMAPbI_3$ (e) Rb(5%)$CsFAMAPbI_3$ (f) Rb(10%)$CsFAMAPbI_3$. Also highlighted in (f) is a phase segregated $RbPbI_3$ grain. Scale bars indicate 200 nm.

S5. Optimization of FETs with different perovskite compositions

In order to optimize the composition of the perovskite for FET performance, we measured different ratio of FA and MA cation in the double cation perovskite which are: $FA_{0.1}MA_{0.9}PbI_3$, $FA_{0.2}MA_{0.8}PbI_3$, $FA_{0.4}MA_{0.6}PbI_3$, $FA_{0.6}MA_{0.4}PbI_3$, $FA_{0.8}MA_{0.2}PbI_3$. Typical transfer characteristics of bottom contact top gate devices measured from different compositions is shown in **figure S11a** and **1c**. Representative output characteristics of MA rich and FA rich compositions are shown in **figure S11 (b&c)**.

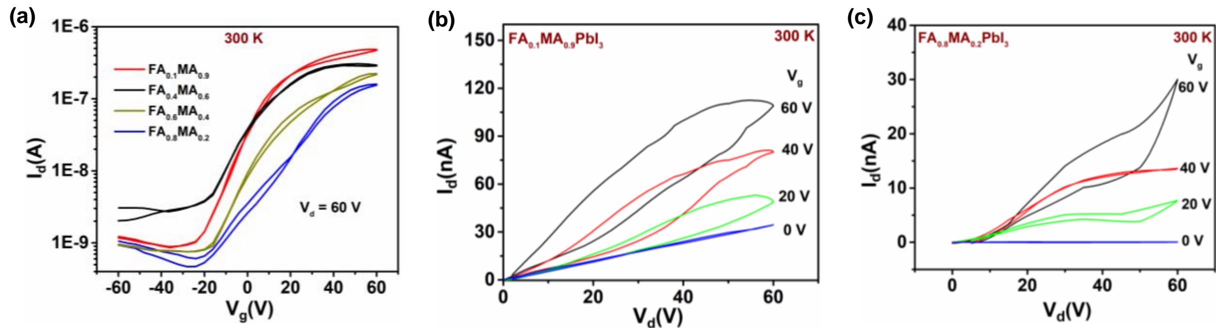

Figure S11: FAMAPbI3 composition optimization. (a) Transfer characteristics; (b) and (c) output characteristics measured on a bottom contact top gate perovskites FET measured at 300 K (L = 100 µm, W = 1mm).

Upon measuring the different composition of FA and MA mixture we observe the optimum characteristics for $FA_{0.2}MA_{0.8}PbI_3$ with μ_{FET} ~ (0.1 ± 0.03) cm^2/Vs. Similar to $MAPbI_3$ FETs, even in this composition of FA and MA mixture we could observe hysteresis-free output characteristics (**figure S12a & b**) and transfer characteristics (**figure S12 c and 1c**) upon increasing the channel length of devices from 20 µm to 100 µm.

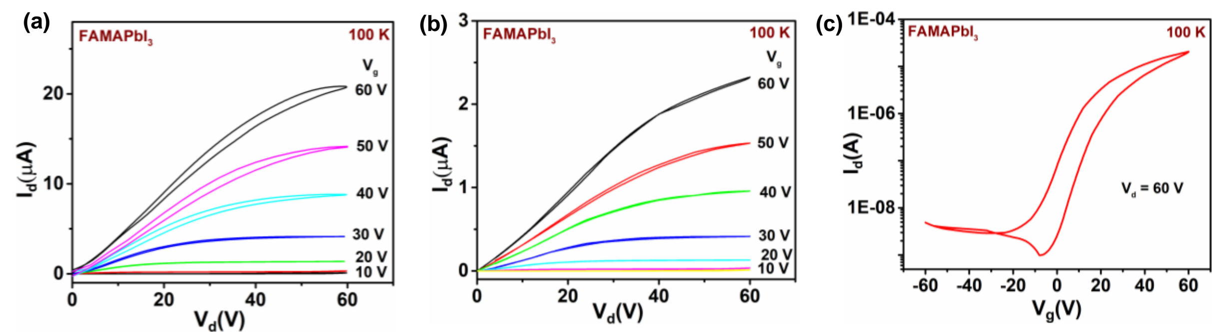

Figure S12: Low temperature characteristics of FAMAPbI3 devices. Output characteristics measured at 100 K on a top-gate, bottom-contact $FAMAPbI_3$ perovskite FETs fabricated with (a) L = 20 µm (b) L = 100 µm. (c) Transfer characteristics measured on the same device with L = 20 µm.

As a next step to optimize the perovskite composition we added 5% molar composition of CsI to the optimized double cation composition resulting in the final perovskite composition of $Cs_{0.05}FA_{0.17}MA_{0.78}PbI_3$. Interestingly we observe this composition to outperform the double cationic $FA_{0.2}MA_{0.8}PbI_3$ composition (**Figure S13a**). In addition, we also measured the triple cationic composition of $Cs_{0.05}FA_{0.78}MA_{0.17}Pb(I_{0.8}Br_{0.2})_3$ that has been widely studied for high efficiency solar cells and observe that it exhibits rather lower ambipolar transport characteristics (10^{-3} cm^2/Vs) than the iodide composition (**Figure S13b**). It is important to note that we have not been able to obtain similar level of device performance with mixed halide based perovskites. Nevertheless, from the reasonably optimized devices we have been able to obtain balanced ambipolar transport which is similar to the reported reference *(28)*. Since it is well known in the field of perovskites that even a small variation in precursor stoichiometry, fabrication condition, spin coating condition have a significant impact on the quality of the perovskite film and thus the device performance. Hence, we believe that to realize high performance triple cation mixed halide based perovskite FETs require future optimization.

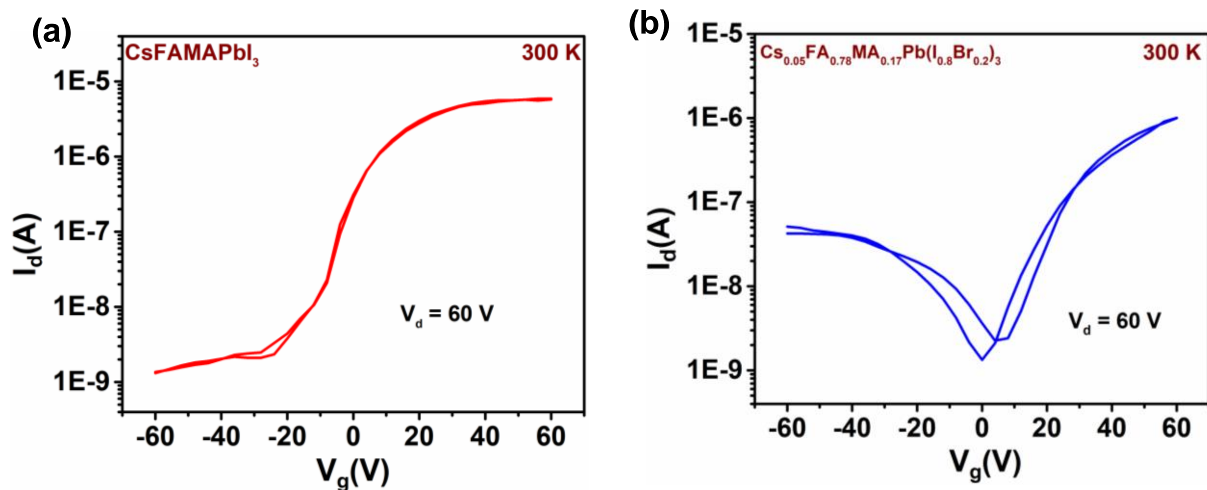

Figure S13: Triple cation perovskite FETs. Representative transfer characteristics measured on top-gate, bottom-contact perovskite FETs fabricated with (a) $CsFAMAPbI_3$ and (b) $Cs_{0.05}FA_{0.78}MA_{0.17}Pb(I_{0.8}Br_{0.2})_3$

RbI was also added in different percentage (1%, 5%, 10%) to $CsFAMAPbI_3$ perovskite for optimization of the device characteristics. Transfer characteristics showing the effect of different Rb composition are shown in **figure S14a and 1e** wherein a degradation in performance is observed upon increasing the Rb concentration to 10% which is consistent with the formation of a phase segregated non perovskite phase as shown in SEM and XRD (**Figure S9** & **S10**). After observing the beneficial effect of Rb passivation on $CsFAMAPbI_3$

transistor performance, K passivated $CsFAMAPbI_3$ perovskites (with K composition varying from 1%, 5% and 10 %) were also investigated in bottom-contact, top-gate perovskite FETs *(37)*. Despite the demonstration of high performance photovoltaic device *(37)* with $KCsFAMAPbI_3$, transfer characteristics shown in **figure S14b** exhibit a decrease in channel current by more than two orders of magnitude upon introduction of even 1% K into $CsFAMAPbI_3$. Upon increasing the K concentration to 10 % no gate modulation was observed in the devices. This decrease in the performance of K passivated $CsFAMAPbI_3$ perovskite could possibly be attributed to the formation of phase segregated non-conducting KI ionic solid at the interface which screens the gate potential thereby reducing the field effect.

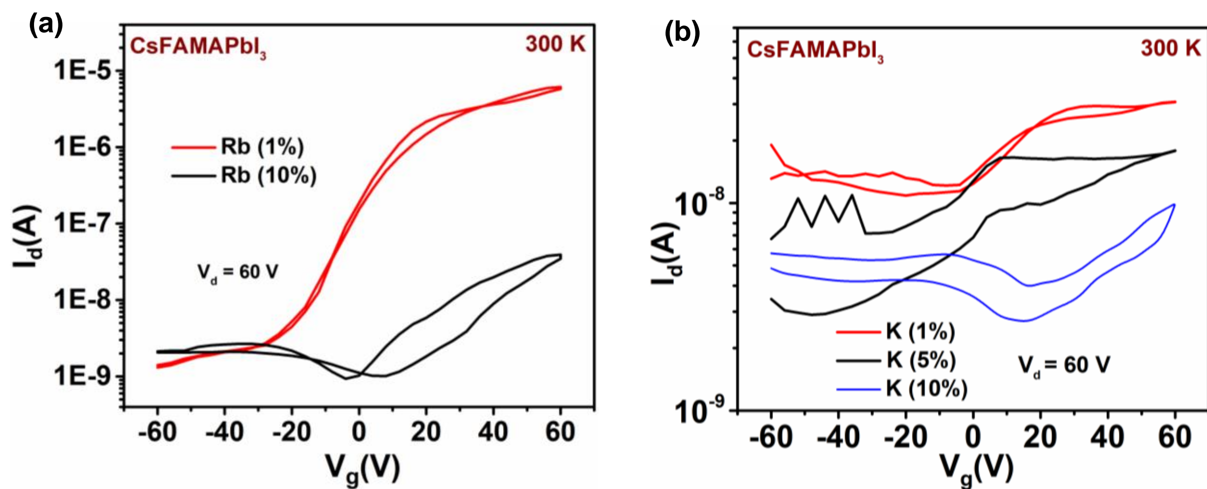

Figure S14: Rb and K passivated triple cation perovskite FETs. Representative transfer characteristics measured on a top-gate, bottom-contact perovskite FETs fabricated with addition of different concentrations of (a) RbI in $CsFAMAPbI_3$ and (b) KI in $CsFAMAPbI_3$.

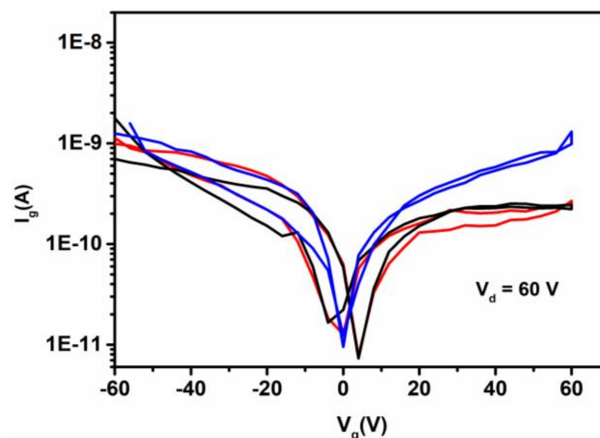

Figure S15: Typical leakage current of the perovskite FETs fabricated with L = 100 µm, W = 1mm.

S6. Temperature dependence of mobility as a function of channel length

The power law behaviour of the $\mu_{FET}(T)$ in the temperature range of 240 K < T < 300 K is attributed to the increase ionic screening of gate potential with an increase in temperature *(25)*. Upon increasing the channel length the effective bias voltage causing the ionic migration decreases. This is also reflected in the $\mu_{FET}(T)$ temperature dependence for temperatures above 240 K which follows a power law ($\mu_{FET} \sim \mu_o T^{-\gamma}$). Upon an increase in channel length from L = 10 µm to L = 100 µm the exponent decreases from 4.1 to 3.5 consistent with a decrease in ionic defect migration under bias (**Figure S16**) which is consistent with decrease in the hysteretic characteristics upon increase in channel length.

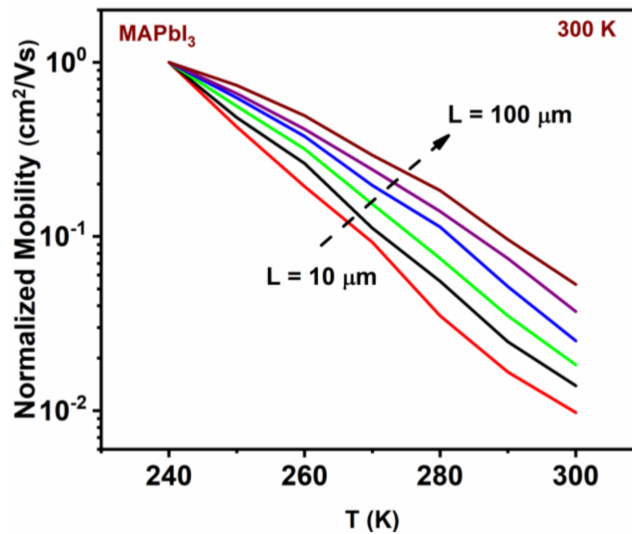

Figure S16: Variation of the normalized μ_{FET} with temperature indicating the reduction of the exponent γ (obtained from the fitting of $\mu_{FET} \sim \mu_o T^{-\gamma}$) from 4.1 to 3.5 upon increasing the L from 10 µm to 100 µm.

S7. Photo-stability Analysis of the perovskite thin films during PL mapping

In general, perovskites are prone to photo degradation. This effect is more pronounced in case of mixed halide perovskites which exhibit halide segregation under illumination. However, the data in the current PL mapping measurements are on iodide based perovskite which are relatively stable towards the formation of non-stoichiometric composition under illumination.

Specifically in our measurements of PL mapping performed on the FET devices, the laser beam is focussed over a local area of the channel (so as to cover at least one pair of source-drain electrodes) and the photoluminescence is measured locally. Since the area illuminated under the laser constituted only a small fraction of the total channel area (0.27 times of the total channel area for devices with $L = 20$ μm and 0.054 time of the total channel area for devices with $L = 100$ μm), hence the effect of the laser illumination on the charge transport of the channel is limited. We also observed another interesting feature during the measurement on $MAPbI_3$ bottom contact bottom gate FETs that when the devices were exposed to laser illumination and continuous voltage bias was applied simultaneously under ambient condition then the devices degraded within 1 minute time. This degradation effect is significantly higher for $MAPbI_3$ devices compared to $RbCsFAMAPbI_3$. Hence, in order to avoid this degradation in our case PL mapping was performed before and after voltage bias (for 180 seconds) while the devices were stored under nitrogen atmosphere.

S8. TGA-DSC analysis

Detailed calorimetric measurements were performed on different lead halide perovskites to estimate the heat of fusion/melting. Thin films required for the measurement were fabricated by drop casting precursor solutions onto ceramic crucibles followed by annealing in-situ at 100 ^{0}C for 30 minutes after which the measurement was performed. In most crystalline materials, the heat of formation and heat of fusion have similar magnitudes with opposite sign. In the present case, the measurement is performed after the formation of the polycrystalline perovskite thin films, hence no peaks corresponding to heat of formation is observed. Upon increasing the temperature it was possible to observe the heat of fusion/melting for the perovskite thin films. Correspondingly, we also observe a mass loss of about (25 – 30 %) in thermogravimetric analysis of all the perovskites which corresponds to weight loss due to the volatilization of CH_3NH_3I and $\frac{1}{2}(I_2)$ and the beginning of decomposition of the perovskite crystal structure (**Figure S17**) *(54)*. Interestingly, it was observed that the enthalpy of fusion increases in the order of $MAPbI_3$ < $FAMAPbI_3$ < $CsFAMAPbI_3$ < $RbCsFAMAPbI_3$ (**table 1).** These observations indicate that relative cohesive energy increases upon cationic substitution.

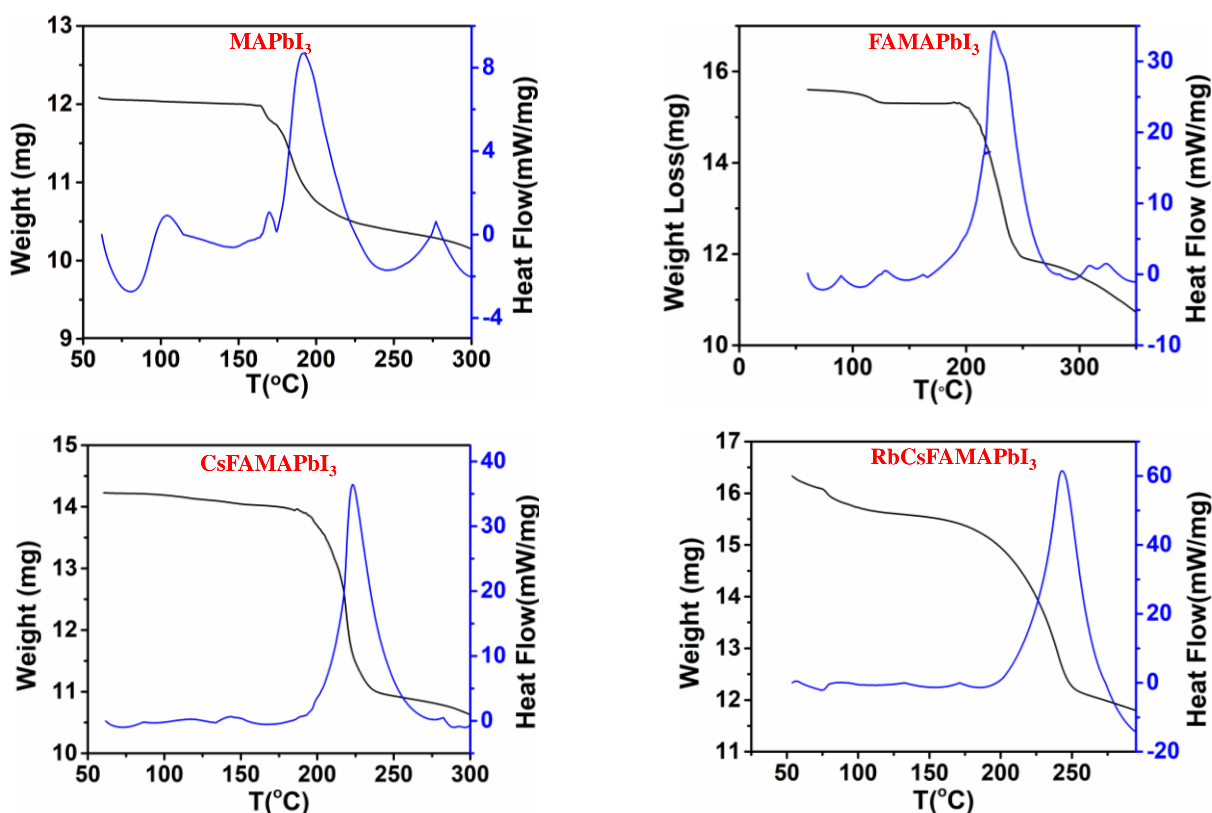

Figure S17: TGA and DSC measurement depicting the melting phase transition and the corresponding weight loss for different perovskite thin films.

Perovskite	Melting Temperature (°C)	Enthalpy of Fusion (J/g)
$MAPbI_3$	191	11.05
$FAMAPbI_3$	224	58.95
$CsFAMAPbI_3$	223	61.60
$RbCsFAMAPbI_3$	243	88

Table 1: Melting Temperature and enthalpy of fusion estimated from the DSC measurements performed on perovskite thin films.

S9. Magnetic susceptibility measurements

Static magnetic measurements were performed on perovskite samples of $MAPbI_3$, $CsFAMAPbI_3$ and Lewis base (methyl acetate) treated samples of $MAPbI_3$ using a SQUID magnetometer over a temperature range of 300 K to 1.8 K. A Magnetization (*M*) versus magnetic field (*H*) plot for a $MAPbI_3$ sample at 300 K is shown in **figure S18a**. Expectedly the sample exhibits a diamagnetic response with a step like discontinuity at T ~ 160 K which corresponds to the orthorhombic to tetragonal phase transition. However, it should be noted that the magnetic response of perovskite samples is a linear sum of contributions from diamagnetic (M_{dia}) and paramagnetic (M_{para}) components. Since the diamagnetic component is temperature independent we can treat the magnetization at 300 K as the baseline to subtract the diamagnetic component and extract the temperature dependent paramagnetic response as a function of temperature (**Figure S18 b &c**). Interestingly the paramagnetic component of magnetization and molar susceptibility measured at 10^4 Oe exhibits a Curie type response which is consistent with the observation of an ESR signal only for temperatures below 50 K. We observe a lower paramagnetic susceptibility (**Figure S18c**) for $CsFAMAPbI_3$ perovskite sample compared to $MAPbI_3$. Considering the fact that paramagnetic response originates from the defects (Pb^{3+} or corresponding generation of iodide vacancy) these measurements are consistent with a lower number of paramagnetic centres or vacancies in $CsFAMAPbI_3$ samples compared to $MAPbI_3$ samples *(43)*.

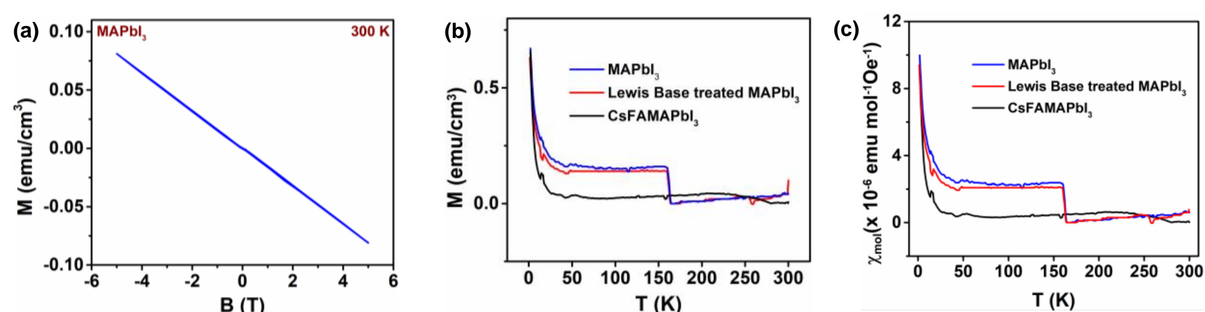

Figure S18: SQUID measurement. (a) Magnetization (M) versus H measured for $MAPbI_3$ samples at 300 K depicting a bulk diamagnetic response. Variation of (b) M and (c) χ_{mol} measured at 1Tesla as a function of T for different perovskite samples. The Lewis base used for the treatment of the samples is methyl acetate in this case.

S10. THz spectroscopy measurements

A typical time domain broadband terahertz (THz) spectroscopy measurement on a $FAMAPbI_3$ perovskite is shown in **figure S19a** (raw data) and the corresponding absorption spectrum in the full range is shown in **figure S19b**. In order to confirm that the peaks and shifts are not because of any artefacts we performed control measurements on bottom-gated, bottom-contact devices without the perovskite layer (**Figure S19c**) which evidently does not exhibit any phonon features, suggesting that the features at ~ 1 THz originate exclusively from the perovskite films. Moreover, the phonon features shown in **figure 19b** is consistent with the reported spectra for lead halide perovskites *(45,46)*.

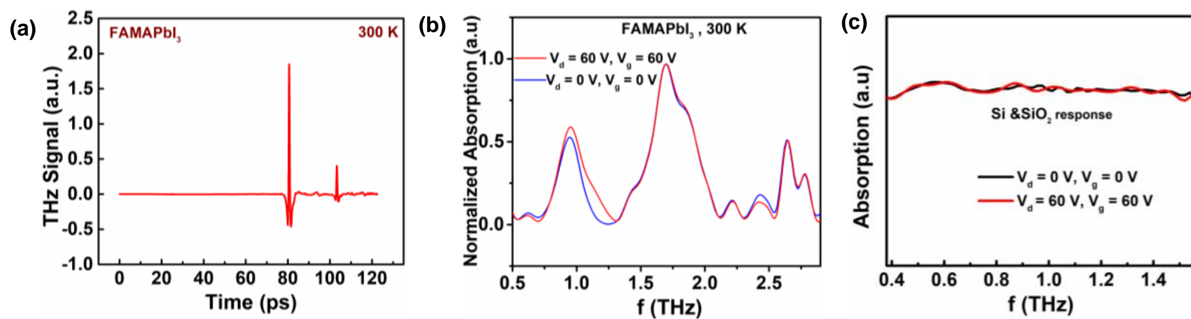

Figure S19: THz spectroscopy. (a) Typical time domain data measured on a bottom contact bottom-gate perovskite transistor (L = 80 µm, W = 19.4 cm) fabricated from $FAMAPbI_3$. (b) Full range absorption spectrum in the THz range obtained from the time domain data; the device was operated under different bias conditions and shows a bias-dependent broadening of the specific phonon band at ~1 THz. (b) Control experiment performed on similar devices without the perovskite layer under similar biasing condition indicating the absence of any phonon modes in the specific range.

In the range of our terahertz absorption measurement, we observe three prominent modes at 1 THz, 1.8 THz and 2.8 THz *(46)*. The peak at 1 THz is attributed to the relaxation of I-Pb-I bond angle which has a mixed transverse and longitudinal optical character whereas the peak at 1.8 THz corresponds to the I-Pb-I relaxation of the inorganic cage through the change in bond length and has longitudinal optical character. The peak at 2.8 THz has a longitudinal optical character and it corresponds to the coupling between the A-cation and the inorganic cage *(46)*. Interestingly, upon biasing the bottom-gate, bottom-contact perovskite device we observe a broadening of the 1 THz peak. Similar observations were made for both $FAMAPbI_3$ and $CsFAMAPbI_3$ perovskite samples as shown in **figure S20**. However, the broadening is significantly decreased for $CsFAMAPbI_3$ and $RbCsFAMAPbI_3$ compared to

$MAPbI_3$ and $FAMAPbI_3$ perovskite-based devices. This is interpreted as a manifestation of the improved structural stability of the lead iodide inorganic cage in $CsFAMAPbI_3$ and $RbCsFAMAPbI_3$ upon application of a bias.

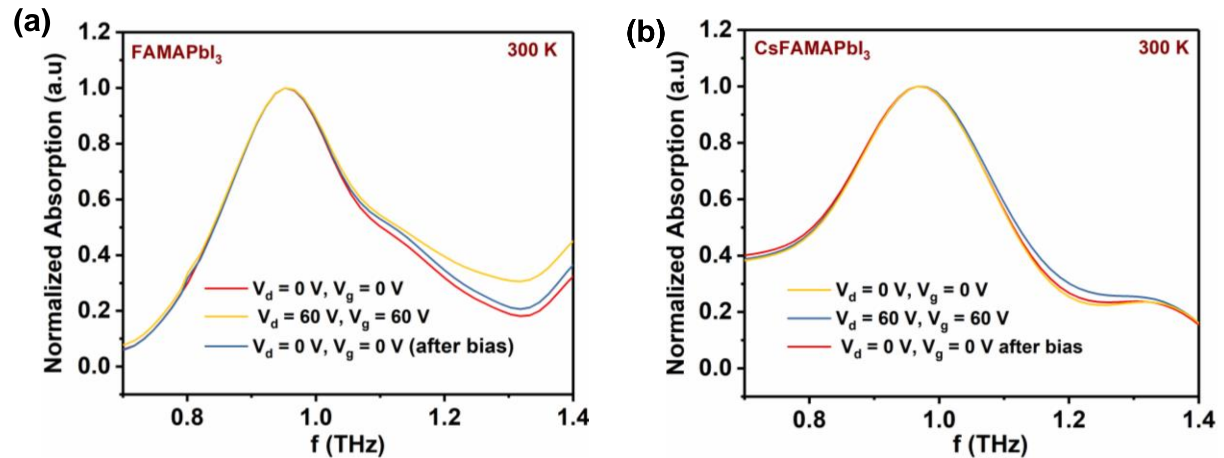

Figure S20: THz absorption measurement on perovskite FETs. Absorption spectra in the THz range measured on a bottom-contact bottom-gate transistor (L = 80 µm, W = 1mm) fabricated using (a) $FAMAPbI_3$ (b) $CsFAMAPbI_3$ perovskite under different biasing condition. Broadening of the phonon mode at 1THz on the high energy side of the peak is observed upon biasing.

Consistent with the decreased broadening of the phonon band close to 1 THz upon biasing we also observe a blue shift in the peak position corresponding to the strengthening of the Pb-I bonding of the inorganic cage as shown in **Figure S21**

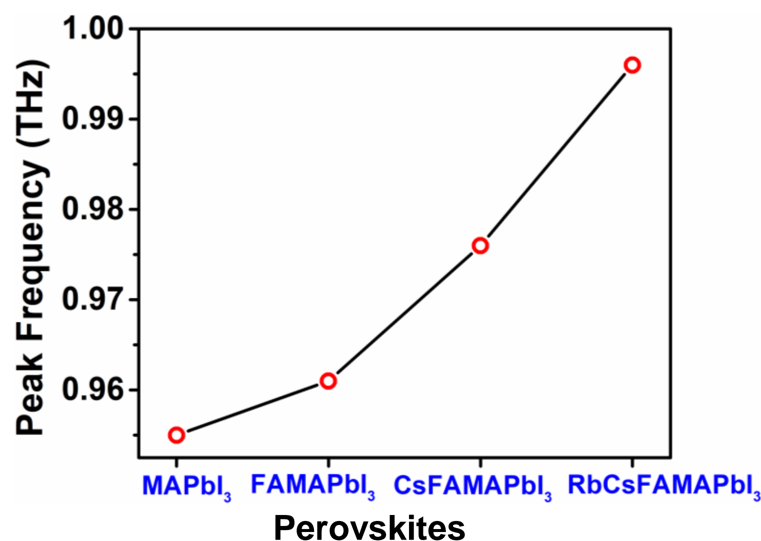

Figure S21: Blue shift in the phonon mode corresponding to I-Pb-I bond indicating the stiffening of the Pb-I octahedron cage upon varying the perovskite layer from $MAPbI_3$ to $RbCsFAMAPbI_3$ in a bottom-contact, bottom-gate device (L = 80 µm, W = 1mm).

To understand the effect of the coupling between the A-cation and Pb-I inorganic cage we probed the broadening of the peak close to 2.8 THz. Devices fabricated from $MAPbI_3$ perovskite layer exhibited a sharpening of the peak at 2.8 THz upon biasing in trans-diode mode ($V_d = V_g = 60$ V) indicating a decrease in entropy of the MA^+ cation (**Figure S22**) consistent with the reported literature *(25)*. Interestingly devices fabricated from $FAMAPbI_3$ perovskite exhibited no variation in the width of the 2.8 THz peak indicating that coupling of the A-cation and Pb- I in-organic cage is significant for polar cations and upon adding a small amount of FA into the perovskite composition it is possible to minimize the coupling between the cation and the inorganic cage.

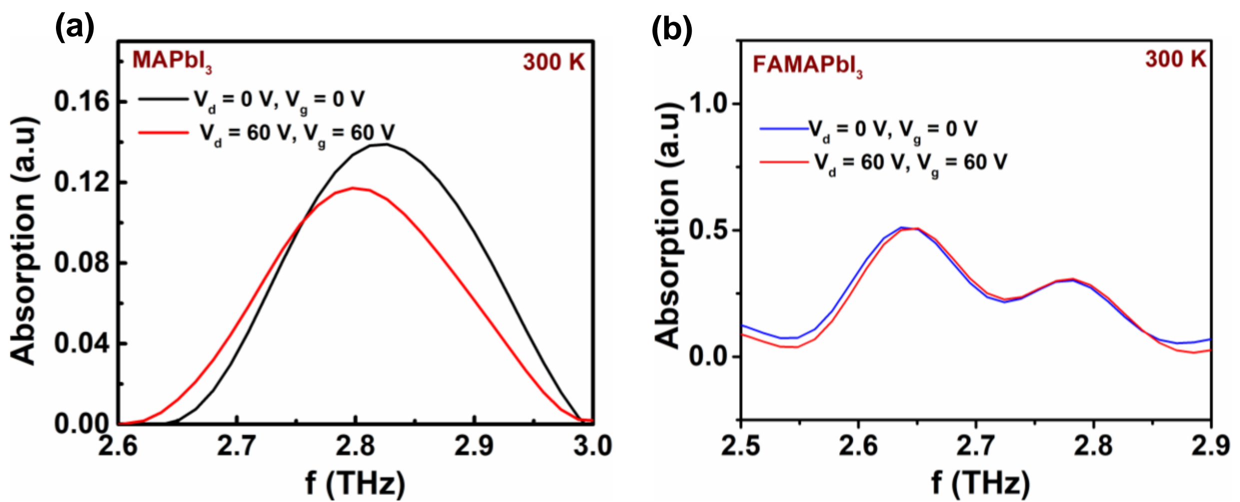

Figure S22: Variation of the 2.6 THz peak upon biasing when measured on bottom-contact, bottom-gate devices fabricated with (a) $MAPbI_3$ and (b) $FAMAPbI_3$ layer.

S11. Water adsorption in perovskites

Upon exposure of a top-gate cytop based $MAPbI_3$ FET to ambient condition for 2 days, the transfer characteristic gradually degrades from n-type to p-type behaviour (**figure S23a**) and after 5 days exhibits a predominantly p-type response. This type of device characteristics is also observed when $MAPbI_3$ precursor solution is obtained with a 5 % excess of PbI_2 (**figure S23b**). This is consistent with the observed decrease in the valence band and conduction band upon utilizing a non-stiochometric composition which modifies the surface of the perovskite layer from intrinsic n-type to p-type *(60)*. Based on this correlation in the transport characteristics we propose that the mechanism for degradation in perovskite FET performance upon exposure to ambient condition involves the formation of excess PbI_2 according to the reaction *(53)*:

$$4\ CH_3NH_3PbI_3 + 4\ H_2O \leftrightharpoons 4\ (CH_3NH_3PbI_3.H_2O) \leftrightharpoons (CH_3NH_3)_4PbI_6.2H_2O + 3PbI_2 + 2\ H_2O$$

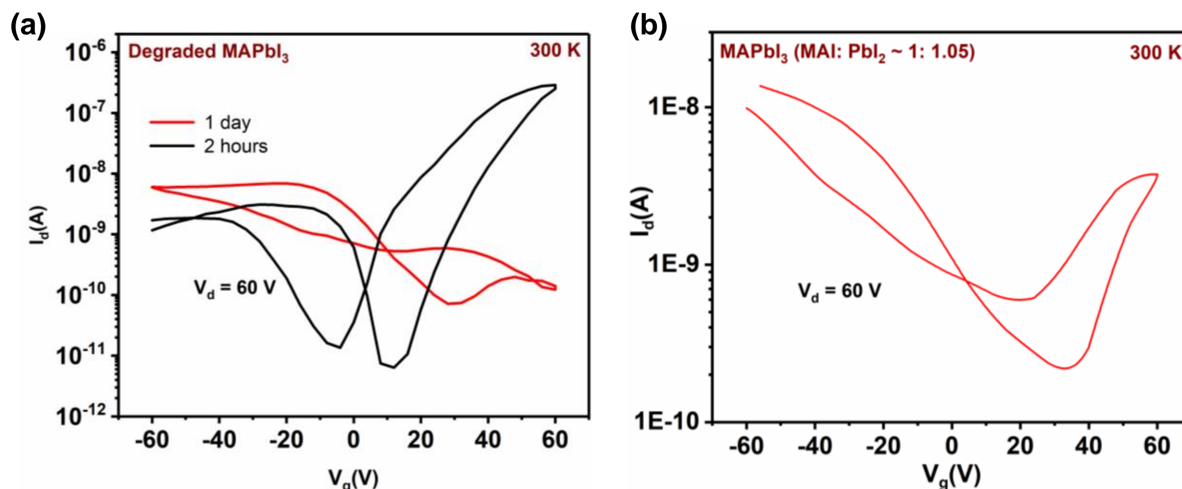

Figure S23: Characterizing degradation of perovskite transistor. (a) Transfer characteristics of a degraded $MAPbI_3$ top-gate bottom-contact device (L = 20 μm, W = 1mm) at 300 K after exposure to ambient condition for 2-5 days. (b) Transfer characteristics measured on top-gate bottom-contact perovskite FET (L = 20 μm, W = 1mm) at 300 K fabricated with a $MAPbI_3$ perovskite containing a 5% excess PbI_2.

Detailed structural analysis of the perovskite thin films was performed to understand the interaction of perovskite semiconductor with ambient moisture. XRD pattern of the pristine perovskite films indicates clean converted perovskite films with un-detectable limits of un-converted PbI_2 (**Figure S24**). However, upon exposure to ambient condition for 2 days, we observe an evolution of phase segregated PbI_2 phase. Note that the relative peak intensity of the PbI_2 peak and the (110) peak of the perovskite decreases in the order $MAPbI_3$ > $FAMAPbI_3$ > $CsFAMAPbI_3$ > $RbCsFAMAPbI_3$ indicating the propensity of PbI_2 formation

of the respective perovskite under ambient conditions. Our analysis thus indicates that Rb based perovskite are most stable against PbI_2 formation under ambient conditions.

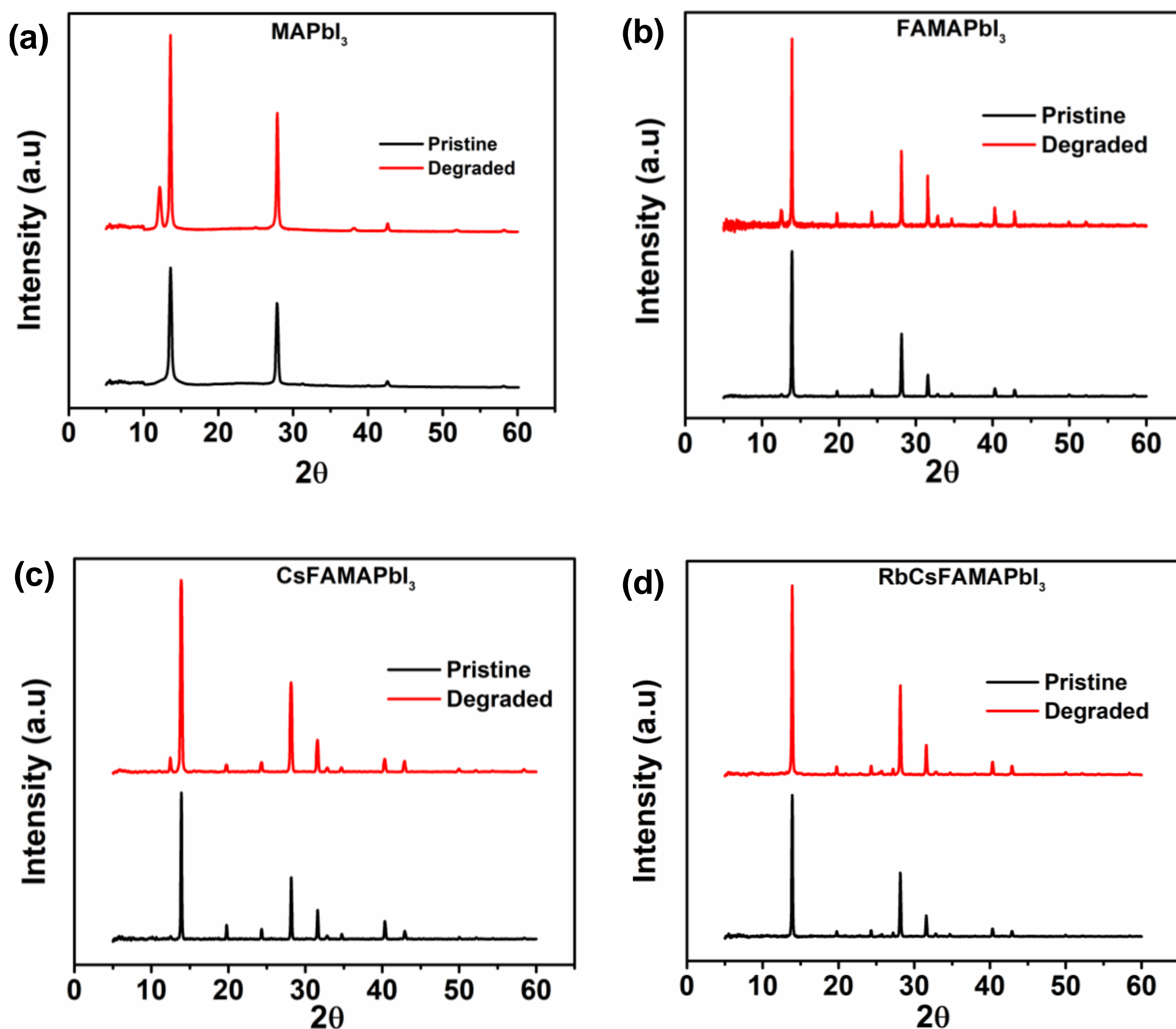

Figure S24: Structural characterization of perovskite degradation. XRD pattern measured on (a) $MAPbI_3$ (b) $FAMAPbI_3$ (c) $CsFAMAPbI_3$ (d) $RbCsFAMAPbI_3$ thin films fabricated on Si substrates depicting the evolution of the PbI_2 peak upon exposure to ambient condition. Note the absence of PbI_2 peak in case of $RbCsFAMAPbI_3$ samples.

To understand the difference in moisture interaction for different perovskites, we performed porosity analysis of the films fabricated from different perovskite layers (details in **Method Section**). Typical Type III N_2 isotherms at 77 K for different perovskite films are shown in **figure S25a** & **b**, which indicate a weak adsorbent-adsorbate interaction and the presence of a small number of mesopores of surface roughness. The most probable pore size of these perovskite thin films was estimated using DFT method *(56)* to be in the range of 4.2

nm to 3.8 nm (**Figure S25c**). Nevertheless, based on these measurements, it is evident that perovskite thin films fabricated from $MAPbI_3$ exhibit the largest volume of adsorbed gas corresponding to higher surface area per unit centimetre square of the substrate area and the smallest surface area is obtained for $RbCsFAMAPbI_3$. This was consistent with the TGA analysis performed on perovskite thin films at temperatures close to 100°C. Note that for a temperature around 100°C mass loss is generally attributed to loss of water molecules as reported earlier *(54)*. We exclude the possibility of residual solvents in this temperature range because these measurements were performed on converted perovskite thin films and the only solvent involved is anhydrous DMF which has a boiling point of 153°C. For $MAPbI_3$ thin films, we observe a weight loss of around 5 % which decreases to < 1 % for $RbCsFAMAPbI_3$ (**Figure S25d**: a zoomed version of TGA curves at **Figure S17**) indicating the relative difference in the moisture adsorption of different perovskite materials.

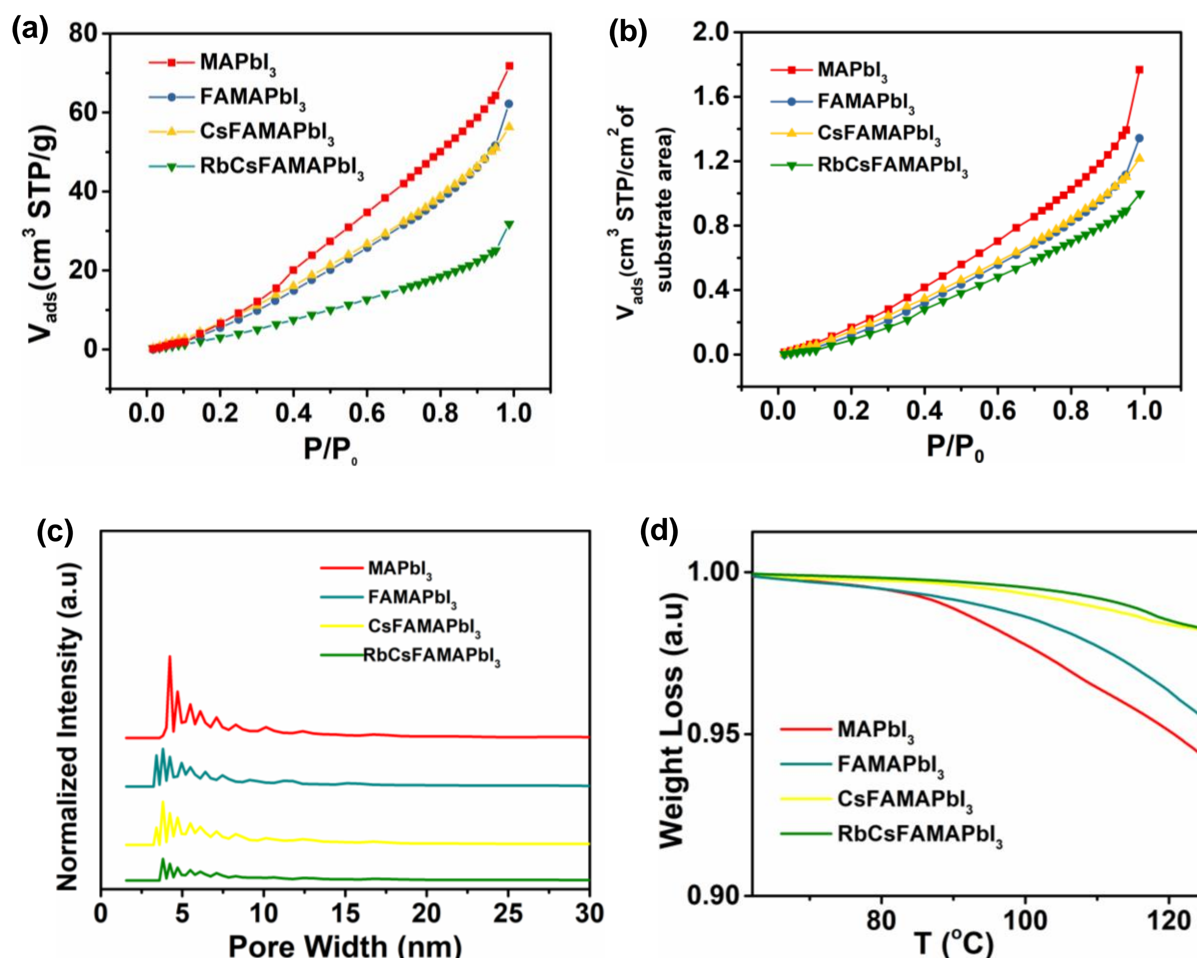

Figure S25: Nitrogen adsorption isotherm. Estimation of the porosity and surface area of perovskite thin film using N_2 adsorption isotherms at 77 K measured as (a) volume of adsorbed N_2 per unit substrate area (b) volume of adsorbed N_2 per unit gram of material plotted as a function of N_2 partial pressure. (c) Pore Size distribution of different perovskite

estimated from the N_2 isotherm measurements.(d) Zoomed TGA plot around 100 ºC depicting the weight loss due to moisture desorption upon heating the thin films of different perovskites.

Detailed structural, thermodynamic and N_2 adsorption isotherm measurements indicate the relative stability of the $RbCsFAMAPbI_3$ perovskite (over a limited time period) structure compared to the conventional $MAPbI_3$ which could possibly correlate to operationally stable high performance perovskite transistor.

S12. Solvent treatment on n-type perovskite semiconductors

a) Lewis Base treatment: When n-type perovskite semiconductor films were treated with Lewis Base and used in a FET, the channel current increases by two orders of magnitude. Correspondingly, the hysteresis behaviour observed in the output characteristics approaches near ideal hysteresis-free characteristic. Consistently, we also observe a decrease in the subthreshold swing (**Figure S26**) . In order to characterize this enhancement in the transport behaviour, we estimated the trapdensity (N_{ss}^{max}) from the subthreshold swing using the expression: $N_{ss}^{max} = \left[SS \times \frac{\log(e)}{\frac{kT}{q}} - 1\right] \times C/q^2$ (where, q is the unit electronic charge and C is the capacitance per unit area of the dielectric layer, *SS* is the subthreshold swing, *k* is the Boltzmann constant). The trap density was estimated to decreases from 10^{13} $cm^{-2}eV^{-1}$ in pristine samples to 10^{12} $cm^{-2}eV^{-1}$ for the solvent treated samples. Note that these values of trap density is higher in comparison to the low trap density of ~ 10^{10} cm^{-3} observed in SCLC measurement of $MAPbI_3$ crystals *(58)*. This behaviour can majorly be attributed to the difference in the SCLC and FET measurement wherein for the later case significant screening of gate potential occurs due to ionic defects. Thus, the complete effect of V_g is not observed in the device characteristics. Moreover, considering the fact that, μ_{FET} versus T trends in FET measurement (in comparison to the hopping behaviour in SCLC measurement) (*59*) exhibits a negative coefficient of mobility, hence typical formulation for trap density estimation based on mobility edge model or hopping mechanism would not be applicable. Under these measurement conditions, the best estimate of the trap density could be obtained from the subthreshold swing of the transfer characteristics. Thus the enhancement in the performance can be attributed to the healing of the iodide vacancies in the perovskite layer upon solvent treatment and in a FET device set unless the ionic defects are completely passivated it would not be possible to probe the inherent bulk defect of the perovskite material.

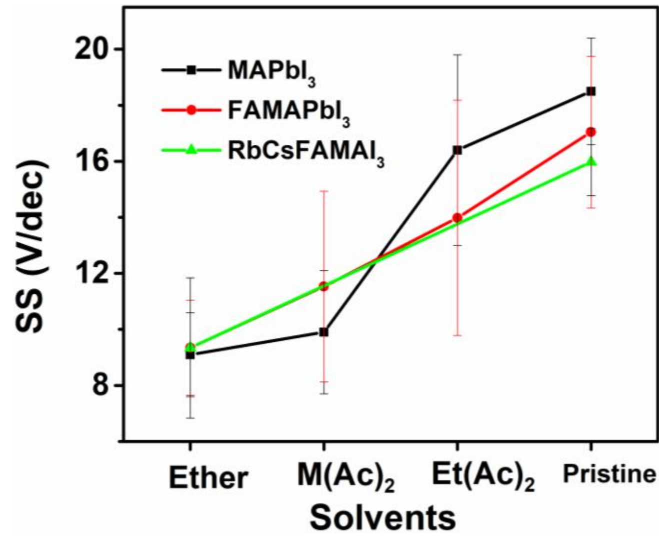

Figure S26: Effect of solvent treatment on FET performance. Variation in the sub-threshold slope estimated from the transfer characteristics measured on a top-gate bottom contact perovskite FET fabricated from different $MAPbI_3$ (black), $FAMAPbI_3$ (red), $RbCsFAMAPbI_3$ (green) perovskites upon treatment with different solvents.

Due to the instabilities observed in the perovskite transistor measurement it is essential to obtain a clean μ_{FET} versus V_g plot so as to ascertain that no overestimation in mobility is observed (**Figure S27a**). In addition to this statistical distribution of the mobility measured on different perovskite based FET and the bias stress instability is provided in **figures S27b** and S26c respectively.

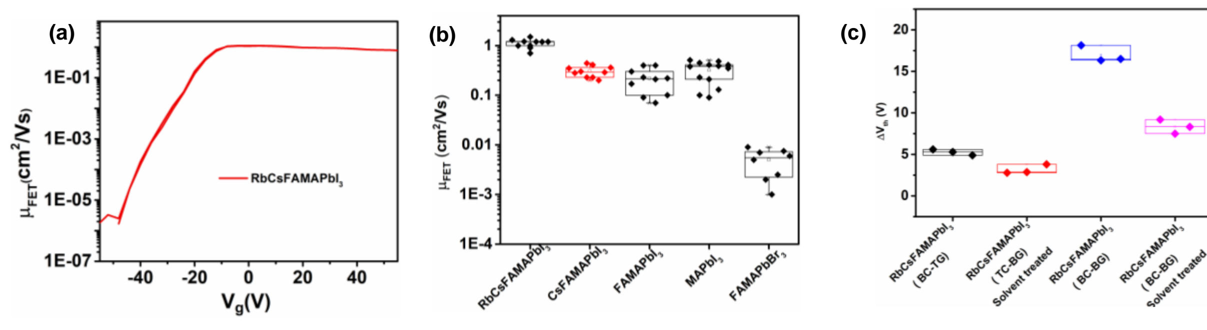

Figure S27: Detailed FET characterization and statistics. (a)μ_{FET} versus V_g plot (b) Statistics of mobility distribution for top-gate bottom contact perovskite FET fabricated from different perovskite FET (L = 100 µm, W = 1mm) after optimization (c) Bias stress statistics for different perovskite FETs. Device outliers are removed from stastistics.

. Upon treating the $RbCsFAMAPbI_3$ perovskite films with Lewis base it was possible to observe hysteresis free output characteristics. However, when the perovskite films were prepared from a precursor solution which was kept in the glovebox for 7 days it was not possible to obtain ideal hysteresis free output characteristics even after Lewis base treatment

of the perovskite films (**Figure S28**). Thus, indicating the importance of using a fresh precursor solution to obtain ideal transistor characteristics.

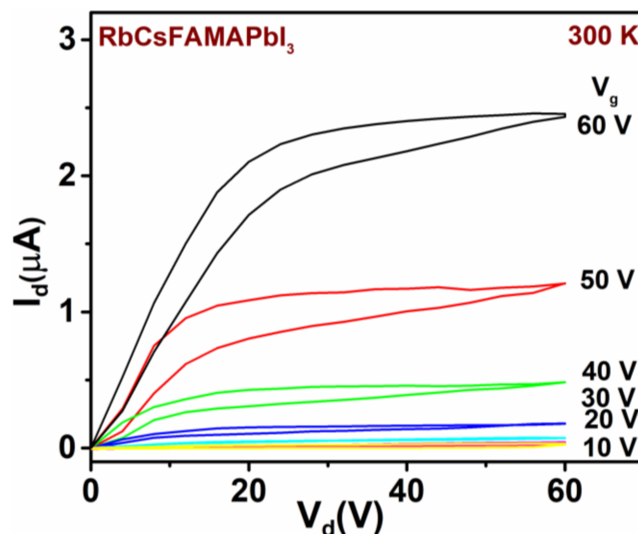

Figure S28: Effect of perovskite precursor ageing on device performance. Output characteristics (at 300 K) measured on a solvent treated bottom contact top-gate RbCsFAMAPbI$_3$ perovskite FET (L = 100 μm, W = 1mm) prepared from a precursor solution prepared 7 days older.

b) Lewis Acid treatment: As a control experiment n-type iodide based perovskite semiconductors were treated with Lewis Acid/π-organic acids. Lewis acids are characterized by the ability to accept electrons. Interestingly upon treating the n-type iodide perovskite surface with Lewis Acids (like: Bromobenzene, tri-nitrobenzene or fomblin) we observe a loss of gate modulation (**Figure S29**) possibly due to creation of electron traps or loss of electronic charges from the interface.

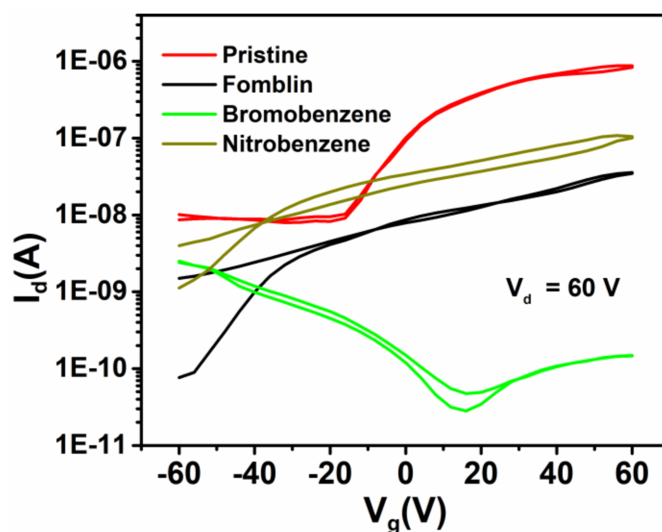

Figure S29: Effect of Lewis acid solvent treatment on $MAPbI_3$ perovskite FETs. Transfer characteristics measured at 300 K on a bottom contact top-gate $MAPbI_3$ perovskite FET (L = 100 µm, W = 1mm) upon treating the perovskite layer with different Lewis/Organic Acids. Bromobenzene: 1,3,5-tri bromo benzene and Nitrobenzene: 1,3,5-trinitrobenzene.

Table 2: Classification of solvents *(57)*

Solvent	**Lewis Acid**	**Lewis Base**	**Azeotrope**
Diethylether		**Y**	**34.2**
Methyl acetate		**Y**	**56.1**
Ethyl Acetate		**Y**	**70.4**
Pyridine		**Y**	**92.6**
Hydrazine		**Y**	**120.3**
Acetic Acid		**Y**	**No**
Fomblin	**Y**		**No**
1,3,5- Trinitrobenzene	**Y**		**98.6**
1,3,5-Tribromobenzene	**Y**		**95.0**

S13. Solvent treatment on p-type perovskite semiconductors

To demonstrate the generality of the solvent treatment technique for p-type perovskite materials we treated p-type $FAMAPbBr_3$ first with Lewis bases like diethyl ether and methylacetate that were found to significantly improve the performance of the n-type devices above.

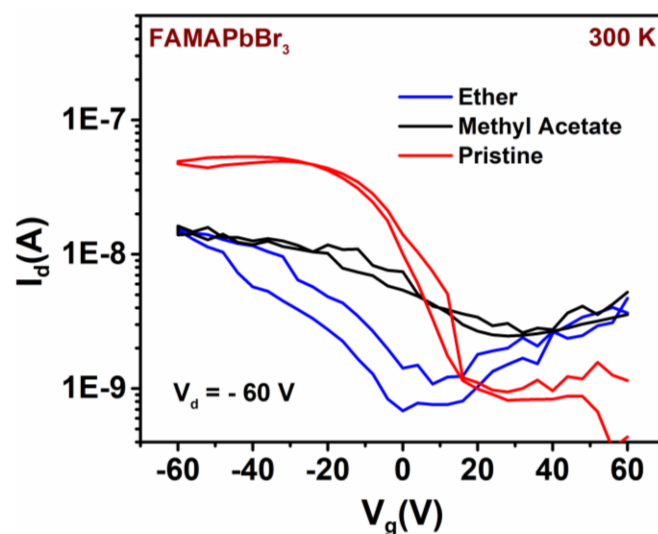

Figure S30: Lewis Base Solvent treatment on $FAMAPbBr_3$ perovskite FETs. Transfer characteristics measured at 300 K on a top gate bottom contact $FAMAPbBr_3$ perovskite FET (L = 100 µm, W = 1mm) upon treating the perovskite layer with different Lewis Bases.

Typical transfer characteristics observed for a bottom-contact, top-gate $FAMAPbBr_3$ device upon treatment with Lewis Base are shown in **figure S30**. Note that despite the fact that these solvents form a positive azeotrope with water we observe a decrease in channel current by at least a factor of 5. Interestingly, when $FAMAPbBr_3$ devices were treated with Lewis/organic Acid 1,3,5-tri bromobenzene the output characteristics exhibit an enhancement in channel current by around 40 times and the current in the transfer characteristics is enhanced by around 20 times with a complete elimination of hysteresis behaviour (**Figure S31a** & **b, 5d**).

It is worth noting that unlike iodide perovskite FETs the transistor performance for bromide devices does not exhibit any improvement upon incorporating Cs as a cation (**Figure S31c**). This trend in bromide based perovskite FETs can possibly be attributed to the increased propensity of CsBr formation which phase segregates and act as non-conducting ionic solid at the perovskite-cytop interface.

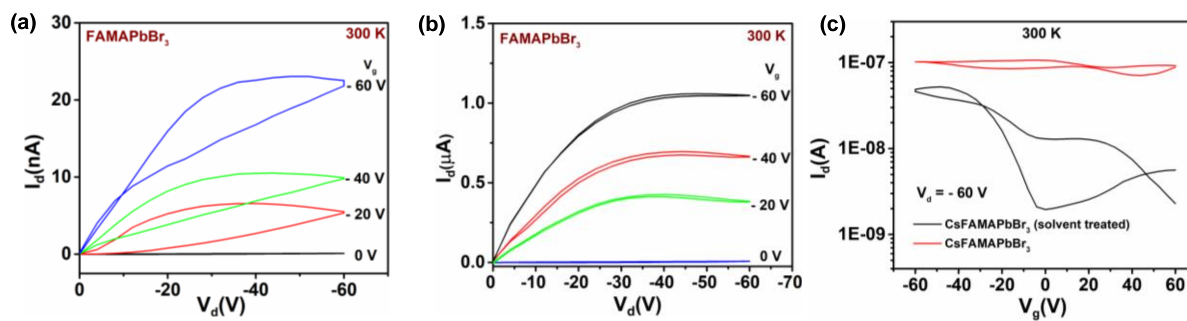

Figure S31: Bromide based perovskite FETs. Output characteristics measured in a top-gate, bottom-contact FET (L = 100 μm, W = 1 mm) at 300 K fabricated using (a) pristine $FAMAPbBr_3$, (b) 1,3,5,tri-bromobenzene treated $FAMAPbBr_3$ (c) pristine $CsFAMAPbBr_3$ (red), 1,3,5,tri-bromo benzene treated $CsFAMAPbBr_3$ (black).

S14. Optimization of bottom contact bottom gate perovskite FETs

The standard solvent based treatment utilized for bottom contact top gate perovskite devices did not result in a significant enhancement in the transistor performance (**Figure S32**), indicating that the effect of solvent is mainly restricted to a few layers on the surface of the films.

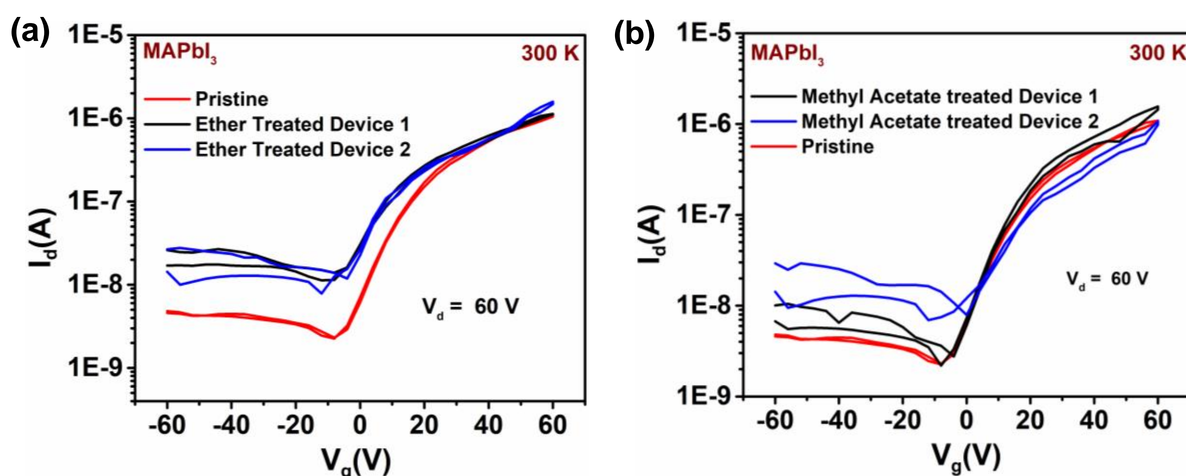

Figure S32: Effect of solvent treatment on bottom contact bottom gated perovskite FETs. Transfer characteristics measured on bottom contact bottom gate perovskite $MAPbI_3$ FETs (L = 100 µm, W = 1 mm) at 300 K upon treatment with different Lewis bases (a) Diethyl ether, (b) methyl acetate.

Bottom-contact bottom gated devices fabricated on SiO_2 treated with ionic layers exhibited rather enhanced performance. A comparison of transistor characteristic of a typical bottom-contact, bottom-gate device with and without interface treatment is shown in **figure 5f** and **S33**.

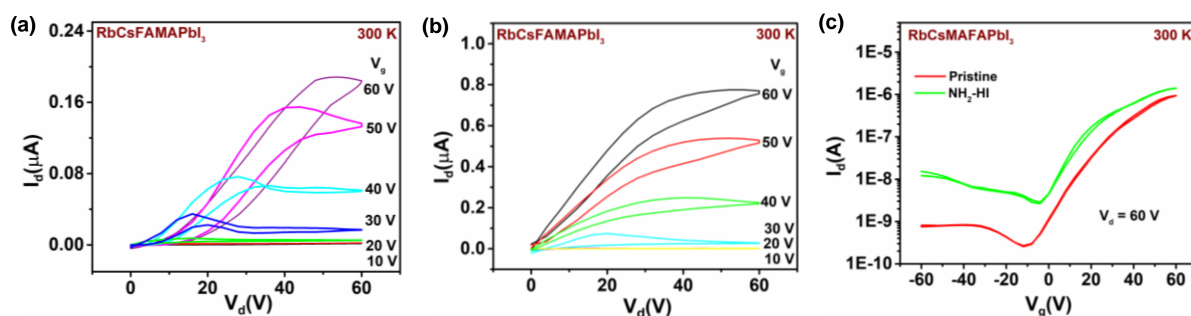

Figure S33: Rb based bottom contact bottom gate perovskite FETs. Output characteristics measured on $RbCsFAMAPbI_3$ based bottom-contact, bottom- gate perovskite FETs (L = 100 µm, W = 1 mm) at 300 K fabricated on (a) pristine Si/SiO_2 and (b) ionic liquid $[BMIM]^+$ $[BF_4]^-$ treated SiO_2 interface (c) transfer characteristics measured on bottom contact bottom gate perovskite devices fabricated with $RbCsFAMAPbI_3$ perovskite on pristine SiO_2 (red) and amine (NH_2-HI) treated self-assembled monolayer (green).

Upon incorporation of divalent cationic salts like ZnI_2 and CdI_2 into $RbCsFAMAPbI_3$ perovskite we observe a decrease in the channel current as shown in **figure S34** (compared to pristine $RbCsFAMAPbI_3$ bottom contact bottom gated devices shown in **Figure S33c**).

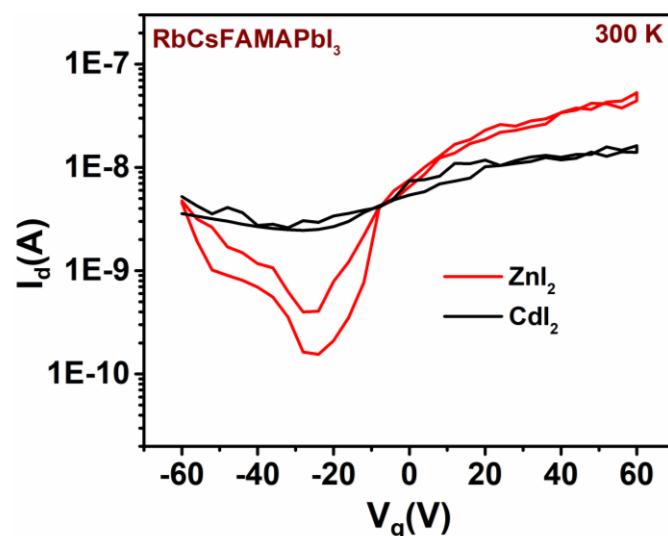

Figure S34: Divalent cationic passivation. Transfer characteristics measured on bottom-contact, bottom-gate perovskite FETs (L = 100 µm, W = 1 mm) at 300 K fabricated with $RbCsFAMAPbI_3$ upon incorporation of 5% composition of divalent cations ZnI_2 (red) and CdI_2 (black).

As a next step, we optimize the performance of a p-type bottom contact bottom gated perovskite transistor fabricated on Si/SiO_2 substrates. Considering the fact that the performance improvement in p-type devices is restricted to Lewis Acid treatment we incorporated divalent additives like Zn^{2+}, Cd^{2+} which behave as soft Lewis Acids into the perovskite.

a) Optimization for $FAMA(PbSn)I_3$ perovskite:

Various compositions of ZnI (1%, 3%, 5% and 10%) and CdI_2 (1%, 3% and 5%) salts were incorporated into $FAMA(PbSn)I_3$. Typical transistor characteristics exhibiting the enhancement in performance upon incorporation of ZnI_2 into $FAMA(PbSn)I_3$ is shown in **figure S35.**

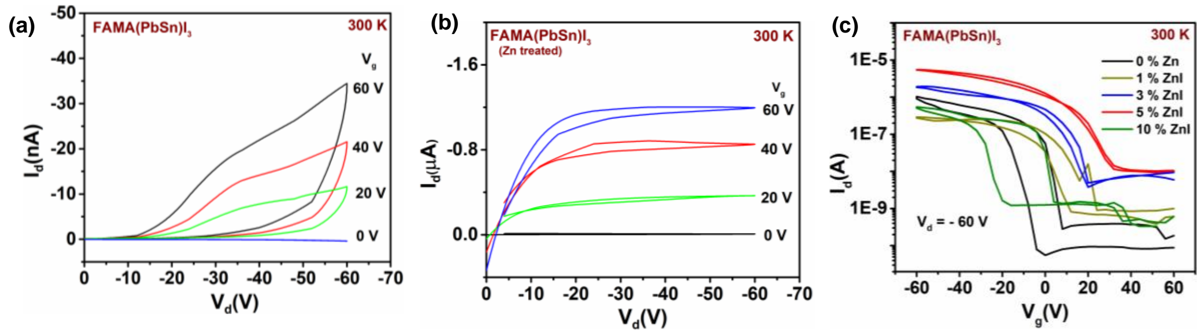

Figure S35: Perovskite FETs with Zn passivation. Output characteristics measured on a bottom-contact, bottom-gate Si/SiO_2 FET (L = 100 µm, W = 1 mm) at 300 K using (a) pristine $FAMA(PbSn)I_3$ (b) ZnI_2 (5% composition) incorporated $FAMA(PbSn)I_3$. (c) Transfer characteristics measured on perovskite devices fabricated with $FAMA(PbSn)I_3$ perovskites incorporated with different amount of Zn composition.

Similar enhancement in transistor characteristics was also obtained upon introduction of CdI_2 salt to $FAMA(PbSn)I_3$ which is shown in **figure S36a.** For bromide based perovskites which also exhibit p-type transistor characteristics, it was possible to obtain enhanced transfer characteristics with the incorporation of $ZnBr_2$.

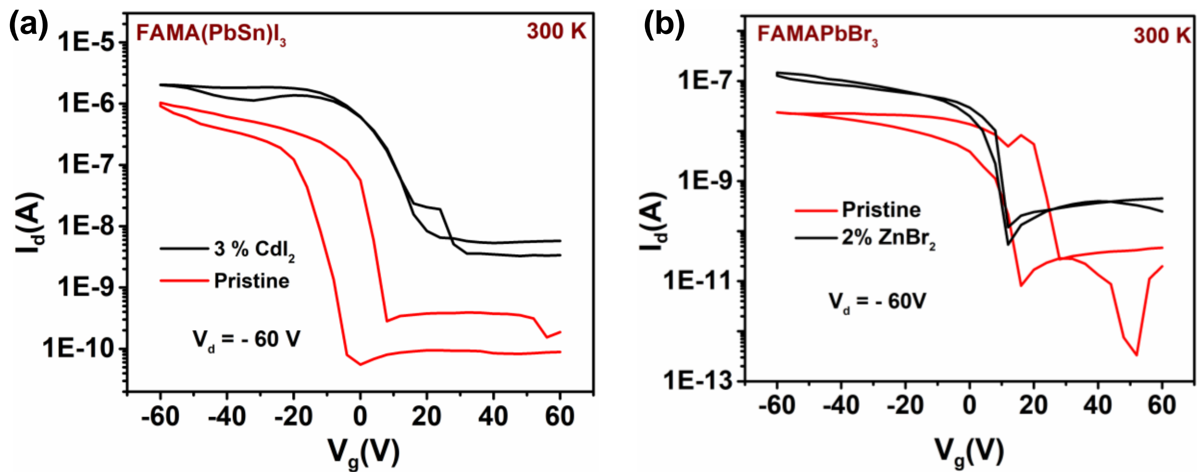

Figure S36: Passivation studies on bottom contact bottom gated perovskite FETs. Comparative transfer characteristics measured on a bottom-contact, bottom-gate Si/SiO_2 FET (L = 100 µm, W = 1 mm) at 300 K using (a) pristine $FAMA(PbSn)I_3$ (red) and 3% CdI_2 incorporated $FAMA(PbSn)I_3$ (b) pristine $FAMAPbBr_3$ (red) and 2% $ZnBr_2$ incorporated $FAMAPbBr_3$.

Correspondingly, upon optimization of the bottom contact bottom gate devices with suitable Lewis base (I^- or F^-) at the interface for n-type perovskite FETs or passivation of Zn^{2+} into the devices it is possible to improve the bias stress stability of the bottom from ΔV_{th}

~ -17 V to ~ -5V for n-type perovskites and ΔV_{th} ~ 14 V to ~ 9 V for p-type perovskite FETs (**Figure S37**).

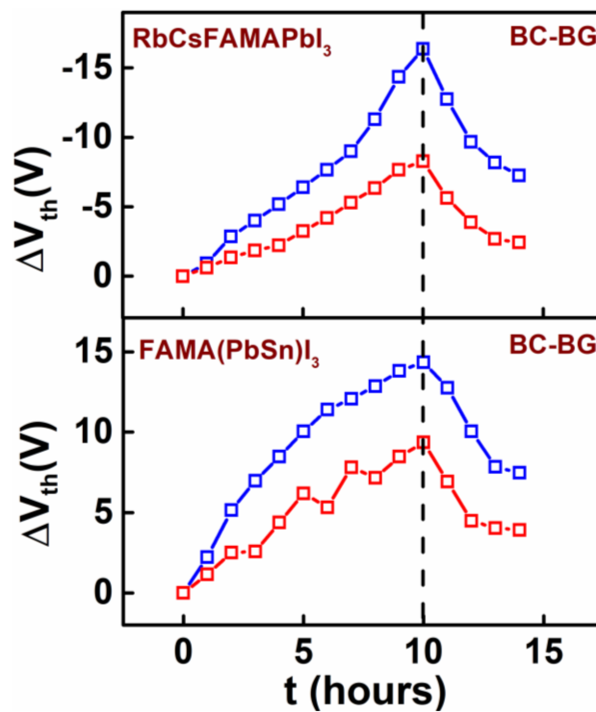

Figure S37: **Bias stability.** Bias endurance measurement on bottom contact bottom gate (BC-BG) FETs fabricated from pristine (blue) and ionic liquid $[BMIM]^+$ $[BF_4]^-$ treated SiO_2 interface (red) for $RbCsFAMAPbI_3$ perovskite layer (top panel) and pristine (blue) as well as 5 % ZnI_2 (red) incorporated $FAMA(PbSn)I_3$ perovskite layer(bottom panel).